



# JWST Reveals Powerful Feedback from Radio Jets in a Massive Galaxy at $z = 4.1$

Namrata Roy<sup>1</sup>, Timothy Heckman<sup>1,2</sup>, Roderik Overzier<sup>3,4,5</sup>, Aayush Saxena<sup>6,7</sup>, Kenneth Duncan<sup>8</sup>, George Miley<sup>3</sup>,  
Montserrat Villar Martín<sup>9</sup>, Krisztina Éva Gabányi<sup>10,11,12,13</sup>, Catarina Aydar<sup>14</sup>, Sarah E. I. Bosman<sup>15,16</sup>, Huub Rottgering<sup>3</sup>,  
Laura Pentericci<sup>17</sup>, Masafusa Onoue<sup>18,19,20</sup>, and Victoria Reynaldi<sup>21,22</sup>

<sup>1</sup> Center for Astrophysical Sciences, Department of Physics and Astronomy, Johns Hopkins University, Baltimore, MD 21218, USA; [nroy13@jhu.edu](mailto:nroy13@jhu.edu)

<sup>2</sup> School of Earth and Space Exploration, Arizona State University, 781 E Terrace Mall, Tempe, AZ 85287, USA

<sup>3</sup> Leiden Observatory, University of Leiden, Niels Bohrweg 2, 2333 CA Leiden, The Netherlands

<sup>4</sup> Observatório Nacional/MCTI, Rua General José Cristino 77, Rio de Janeiro, RJ 20921-400, Brazil

<sup>5</sup> TNO, Oude Waalsdorperweg 63, 2597 AK, Den Haag, The Netherlands

<sup>6</sup> Department of Physics, University of Oxford, Denys Wilkinson Building, Keble Road, Oxford OX1 3RH, UK

<sup>7</sup> Department of Physics and Astronomy, University College London, Gower Street, London WC1E 6BT, UK

<sup>8</sup> Institute for Astronomy, University of Edinburgh Royal Observatory, Blackford Hill, Edinburgh EH9 3HJ, UK

<sup>9</sup> Centro de Astrobiología (CAB), CSIC-INTA, Ctra. de Ajalvir, km 4, 28850 Torrejón de Ardoz, Madrid, Spain

<sup>10</sup> Department of Astronomy, Institute of Physics and Astronomy, ELTE Eötvös Loránd University, Pázmány Péter sétány 1/A, H-1117 Budapest, Hungary

<sup>11</sup> HUN-REN-ELTE Extragalactic Astrophysics Research Group, Eötvös Loránd University, Pázmány Péter sétány 1/A, H-1117 Budapest, Hungary

<sup>12</sup> Konkoly Observatory, HUN-REN Research Centre for Astronomy and Earth Sciences, Konkoly Thege Miklós út 15-17, H-1121 Budapest, Hungary

<sup>13</sup> CSFK, MTA Centre of Excellence, Konkoly Thege Miklós út 15-17, H-1121 Budapest, Hungary

<sup>14</sup> Max-Planck-Institut für Extraterrestrische Physik, Gießenbachstraße, D-85748 Garching, Germany

<sup>15</sup> Institute for Theoretical Physics, Heidelberg University, Philosophenweg 12, D-69120 Heidelberg, Germany

<sup>16</sup> Max-Planck-Institut für Astronomie, Königstuhl 17, D-69117 Heidelberg, Germany

<sup>17</sup> INAF—Osservatorio Astronomico di Roma, via Frascati 33, 00078, Monteporzio Catone, Italy

<sup>18</sup> Kavli Institute for the Physics and Mathematics of the Universe (Kavli IPMU, WPI), The University of Tokyo, 5-1-5 Kashiwanoha, Kashiwa, Chiba 277-8583, Japan

<sup>19</sup> Center for Data-Driven Discovery, Kavli IPMU (WPI), UTIAS, The University of Tokyo, Kashiwa, Chiba 277-8583, Japan

<sup>20</sup> Kavli Institute for Astronomy and Astrophysics, Peking University, Beijing 100871, People's Republic of China

<sup>21</sup> Instituto de Astrofísica de La Plata, CONICET-UNLP, CCT La Plata, Paseo del Bosque, B1900FWA La Plata, Argentina

<sup>22</sup> Facultad de Ciencias Astronómicas y Geofísicas, Universidad Nacional de La Plata, Paseo del Bosque, B1900FWA La Plata, Argentina

Received 2023 December 7; revised 2024 May 9; accepted 2024 May 13; published 2024 July 19

## Abstract

We report observations of a powerful ionized gas outflow in the  $z = 4.1$  luminous radio galaxy TNJ1338-1942 hosting an obscured quasar using the Near Infrared Spectrograph (NIRSpec) on board JWST. We spatially resolve a large-scale ( $\sim 15$  kpc) outflow and measure outflow rates. The outflowing gas shows velocities exceeding  $900 \text{ km s}^{-1}$  and broad line profiles with widths exceeding  $1200 \text{ km s}^{-1}$  located at an  $\sim 10$  kpc projected distance from the central nucleus. The outflowing nebula spatially overlaps with the brightest radio lobe, indicating that the powerful radio jets are responsible for the outflow kinematics. The gas is possibly ionized by the obscured quasar with a contribution from shocks induced by the jets. The mass outflow rate map shows that the region with the broadest line profiles exhibits the strongest outflow rates. The total mass outflow rate is  $\sim 500 M_{\odot} \text{ yr}^{-1}$ , and the mass loading factor is  $\sim 1$ , indicating that a significant part of the gas is displaced outwards by the outflow. Our hypothesis is that the overpressured shocked jet fluid expands laterally to create an expanding ellipsoidal “cocoon” that causes the surrounding gas to accelerate outwards. The total kinetic energy injected by the radio jet is about 3 orders of magnitude larger than the energy in the outflowing ionized gas. This implies that kinetic energy must be transferred inefficiently from the jets to the gas. The bulk of the deposited energy possibly lies in the form of hot X-ray-emitting gas.

*Unified Astronomy Thesaurus concepts:* AGN host galaxies (2017); Active galaxies (17); Giant radio galaxies (654); Galactic winds (572); Emission line galaxies (459); Radio lobes (1348)

## 1. Introduction

### 1.1. Background

Supermassive black holes, which are ubiquitous in the nuclei of galaxies, play a crucial role in the evolution of galaxies. Large-scale cosmological simulations found that without incorporating energy released from active galactic nuclei (AGN), massive galaxies overproduce young stars and fail to truncate star formation in time (Di Matteo et al. 2005; Croton et al. 2006). Thus, they are unable to reproduce the galaxy

population we observe today. However, the detailed mechanism regarding this feedback process is still unknown.

AGN can provide feedback to their surrounding environments through a variety of processes, including direct radiation (Ciotti et al. 2010), relativistic plasma jets (Fabian 2012), and massive outflows of gas (Crenshaw et al. 2003). These energy outputs are sufficient to unbind or reheat most of the interstellar gas, if the energy is deposited efficiently in the ambient medium. In the context of galaxy evolution, there are two proposed feedback channels depending on the mode of energy transfer: winds driven as part of the bolometrically luminous “quasar” mode (Di Matteo et al. 2005), and the “radio” or the kinetic mode (Croton et al. 2006; McNamara & Nulsen 2007) where the primary means of energy transfer is via radio jets traced by emission from relativistically charged particles. Multiple observations have provided evidence of powerful

high-velocity outflows in both these modes (Maiolino et al. 2012; Cicone et al. 2015; Jarvis et al. 2021; Morganti et al. 2021; Speranza et al. 2021; Villar Martín et al. 2021). Recently, Heckman & Best (2023) computed a global inventory of both feedback modes, and concluded that the radio-jet mode is likely to be a more important mechanism.

Our detailed understanding of how radio jets impact the host galaxy interstellar medium (ISM) has made considerable progress in recent years using hydrodynamical jet simulations (Wagner & Bicknell 2011; Wagner et al. 2012; Mukherjee et al. 2018, 2020; Dutta et al. 2023). These models indicate that collimated radio jets effectively deposit energy and momentum as they plow through the low-density channels of the ISM. Eventually, they inflate large cocoons/bubbles of shocked gas that can entrain the ambient gas leading to large-scale outflows and a kinematically disturbed ISM (Begelman & Cioffi 1989). This scenario is in agreement with observations of nearby radio-AGN systems, which exhibit irregular ionized gas kinematics in the host galaxy ISM (Wagner et al. 2012; Mukherjee et al. 2016; Roy et al. 2018, 2021; Girdhar et al. 2022; Meenakshi et al. 2022). Similar observations of outflows driven by powerful radio galaxies at high redshift ( $z > 2$ ) exist (Nesvadba et al. 2017), but are comparatively rare.

High-redshift radio galaxies (HZRGs) are excellent laboratories for studying AGN feedback during the late stages of massive galaxy evolution in the early Universe. They have high stellar masses, large star formation rates (SFRs; exceeding a few hundred to often a thousand solar masses per year), and host powerful radio jets. These jets are often cospatial with extended warm ionized gas nebulae spanning several tens of kiloparsecs. The host ISMs of radio galaxies observed at  $z > 2$  show evidence of large velocity offsets, broad lines, and disturbed kinematics (Villar-Martín et al. 2003; Nesvadba et al. 2006, 2008, 2017). Since these HZRGs are thought to host luminous obscured quasi-stellar objects (QSOs), the blinding glare of light from the central AGN is blocked. So it is straightforward to identify broad lines associated with outflowing gas in the galaxy’s ISM.

### 1.2. Our Target: TNJ1338-1942

The luminous HZRG TNJ1338-1942 (hereafter TNJ1338; De Breuck et al. 1999) is one of the most powerful radio sources known in the early Universe ( $L_{1.4 \text{ GHz}} \sim 10^{28.3} \text{ W Hz}^{-1}$  at  $z = 4.104$ ) and one of the first  $z > 4$  radio galaxies to be discovered in the southern sky. The radio spectral index of this source is ultrasteepest ( $S_\nu \propto \nu^{-1.6}$ ; Pentericci et al. 2000), as calculated between observing frequencies of 4.5 GHz and 8.2 GHz (i.e., emitting frequencies of 23 GHz and 42 GHz, respectively). The radio morphology from the Very Large Array (VLA) indicates a double-lobed structure with a projected end-to-end size of 36 kpc. The radio image is dominated by radio lobes/hot spots with no visible radio jets connecting them with the host galaxy, which resembles a typical FR II radio galaxy at high redshift with a steep spectral index. The radio “core” is not detected at 4.5 GHz, and there is a marginal  $< 3\sigma$  emission near the core in the 8.2 GHz radio image although it does not appear to be spatially coincident with the nucleus of the host galaxy. Based on the 4.5 GHz and 8.2 GHz images, Pentericci et al. (2000) estimated the core spectral index to be  $-1.0$ , although the number is highly uncertain owing to the marginal detection of the radio core. The brightest radio lobe is located 8.8 kpc north of the host galaxy

and the fainter one is 27.7 kpc to the south (Figure 1, left panel). The northern radio lobe is  $\sim 4$  times brighter than the southern component. The host galaxy resides at the core of a significant overdensity of galaxies, indicating the presence of a protocluster (Venemans et al. 2002; Miley et al. 2004; Zirm et al. 2005; Intema et al. 2006; Overzier et al. 2008, 2009; Saito et al. 2015). TNJ1338 also has a 30 kpc sized region of X-ray emission detected with Chandra X-ray observations, coincident with the radio emission, which is suggested to be due to inverse Compton scattering of photons by relativistic electrons around the radio AGN (Smail & Blundell 2013). MUSE observations reveal an extremely luminous ( $L_{\text{Ly}\alpha} \sim 4 \times 10^{44} \text{ erg s}^{-1}$ ) and spatially asymmetric giant Ly $\alpha$  halo (De Breuck et al. 1999; Venemans et al. 2002; Swinbank et al. 2015), which spans a massive scale of  $\sim 150$  kpc, and is spatially offset from the radio and X-ray emission. Also, this radio galaxy hosts a central obscured quasar detected in the infrared continuum (Falkendal et al. 2019) and traced by very luminous optical emission lines. Although ground-based near-infrared integral field unit (IFU) observations using the Very Large Telescope SINFONI instrument do not spatially resolve this emission region (Nesvadba et al. 2017), they show broad line profiles ( $\sim 10^3 \text{ km s}^{-1}$ ), implying a powerful outflow (see also De Breuck et al. 1999; Swinbank et al. 2015).

This unique conglomeration of multiwavelength properties in such a high-redshift radio-loud source made TNJ1338 a prime target for JWST observations. TNJ1338 was observed with JWST NIRCAM as part of a Cycle 1 imaging program (GTO 1176, PI: Windhorst; Duncan et al. 2023; Windhorst et al. 2023) and also observed with JWST Near Infrared Spectrograph (NIRSpec) IFU to obtain spatially resolved rest-frame optical spectroscopy (General Observer (GO) program 1964, PIs: Overzier and Saxena, Saxena et al. 2024). Deep optical imaging from HST/ACS observations spatially resolved the optical emission tracing extended ionized gas in this galaxy. It revealed that the ionized gas structure is clumpy (Miley et al. 2004; Zirm et al. 2005). JWST NIRCAM images confirmed this finding, stating that there is indeed abundant extended ionized emission, and it consists of two distinct components: one centered on the host galaxy center (marked as “H” in Figure 1 right), and the other nebular component roughly spatially coincident with the bright northern radio lobe (marked as “N” in Figure 1 right; Duncan et al. 2023). The encounter of the northern jet with the denser gas in the north is a possible reason why the northern radio lobe is brighter and much closer to the host galaxy nucleus than the southern lobe.

### 1.3. Questions to Be Investigated

In this work, we utilize the NIRSpec IFU observations to study the spatially resolved ionized gas kinematics in the host galaxy (H) and nebular-line-dominated region (N) to investigate how the radio jets interact with the ambient medium, and if the outflow energetics are sufficient to provide large-scale feedback in this high-redshift radio source. A companion paper (Saxena et al. 2024) discusses the ionization structure of this galaxy in detail.

The impact of the outflow on the host galaxy ISM can be quantified by measuring the outflowing mass ( $M$ ), mass outflow rate ( $\dot{M}$ ), outflow velocity ( $v$ ), momentum flow rate ( $\dot{p} = \dot{M}v$ ), and the kinetic power of the emission-line gas ( $\dot{E} = \frac{1}{2}\dot{M}v^2$ ) of the outflows. Simulations indicate that efficient feedback with high coupling with the ISM needs a kinetic power of outflows

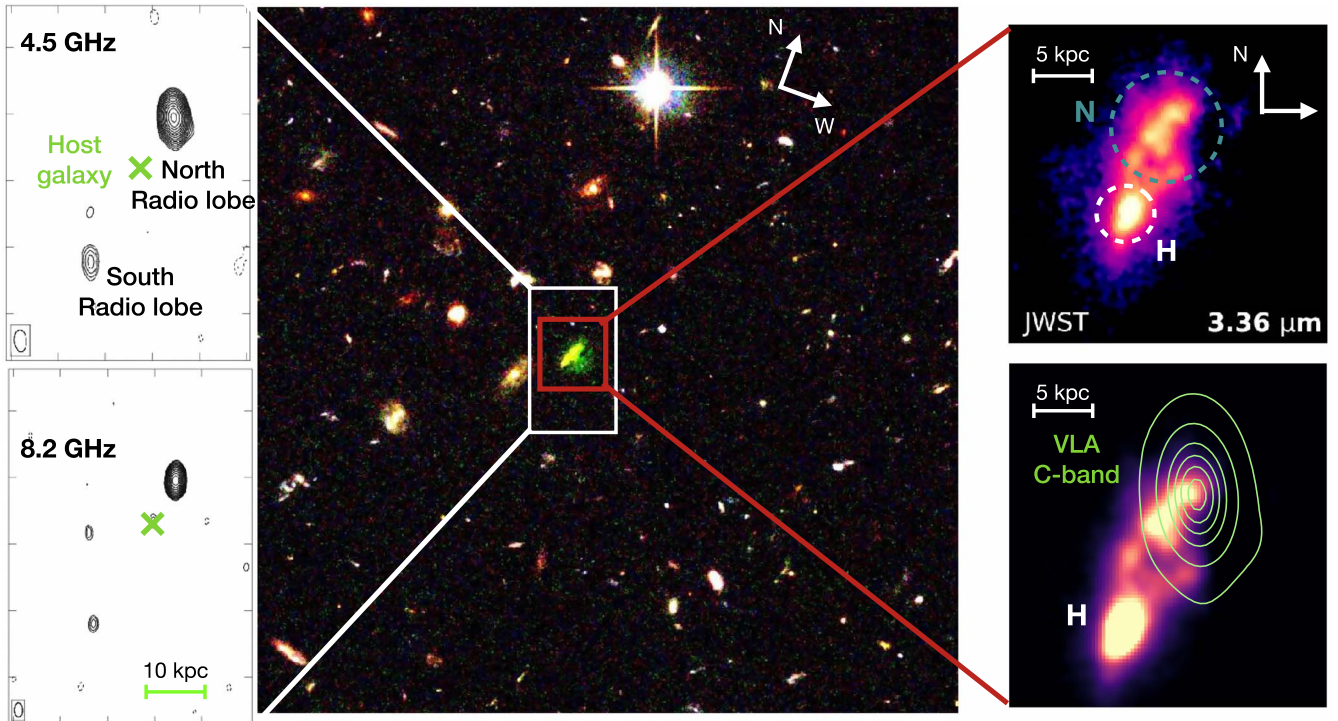


**Figure 1.** Middle: color-composite image from the Hubble Space Telescope (HST) Advanced Camera for Surveys (ACS) Wide Field Camera, with our radio galaxy TNJ1338 highlighted in the center (Miley et al. 2004). Left: VLA continuum map at 4.5 GHz (top left) and at 8.2 GHz (bottom left) from Pentericci et al. (2000), with the host galaxy position marked as a green cross. TNJ1338 exhibits a double-lobed radio source with the northern lobe about  $\sim 4$  times brighter than the southern lobe. Top right: the JWST Near Infrared Camera (NIRCAM)/F335M image around the northern radio lobe (Duncan et al. 2023) reveals two distinct components: a compact host galaxy (“H”), and an extended clumpy emission-line-dominated nebular (“N”) region. Bottom right: a color-composite image which combines the HST ACS imaging and the NIRCAM imaging (Duncan et al. 2023). “H” indicates the host galaxy continuum. Overlaid green contours show the VLA radio continuum emission at 4.5 GHz from the northern radio lobe with contours showing 1%, 10%, 30%, 50%, 70%, and 90% of the peak intensity (Pentericci et al. 2000). The bright northern radio lobe is spatially coincident with the nebular-emission-line-dominated region.

to be at least 0.5–5% of the AGN bolometric luminosity (Di Matteo et al. 2005; Hopkins & Elvis 2010). Studies of narrow-line region outflows in nearby Seyferts/QSOs have measured a large range of kinetic efficiency  $\dot{E}/L_{\text{bol}}$  from  $<0.1\%$  to as high as 10% for outflows in ionized phases (Brusa et al. 2016; Fiore et al. 2017; Baron & Netzer 2019; Dall’Agnol de Oliveira et al. 2021), and an even larger range in mass outflow rates ( $0.01 - 10^3 M_{\odot} \text{ yr}^{-1}$ ). The majority of these studies have measured “global” outflow rates and power with single mass, velocity, and density estimates (Harrison et al. 2014; McElroy et al. 2015; Kakkad et al. 2016; Villar-Martín et al. 2016). Many of these measurements are derived from seeing-limited observations, and the outflow sizes and rates are massively overestimated. Moreover, these integrated measurements result in an oversimplification of the kinematically complex systems and often result in up to 3 orders of magnitude uncertainties in the calculated AGN kinetic power (Villar-Martín et al. 2016; Revalski et al. 2018; Storchi-Bergmann et al. 2018). Spatially resolved observations are thus necessary to map out the spatial distribution of outflow velocities, densities, and ionized gas masses and to thus better constrain the outflow parameters as a function of spatial position (Crenshaw et al. 2015; Revalski et al. 2018; Venturi et al. 2018; Revalski et al. 2021; Kakkad et al. 2022).

Here we report the first measurements of spatially resolved outflow rates and energetics from a  $z > 4$  radio galaxy using JWST, utilizing key rest-frame optical features as ionized gas tracers. We find that TNJ1338 shows spatially extended ionized gas with large-scale outflowing gas kinematics with outflow

velocities  $v_{\text{outflow}} \sim 800 - 1000 \text{ km s}^{-1}$ , and line widths at 80% of the emission-line flux ( $W_{80}$ ) exceeding  $2000 \text{ km s}^{-1}$ . The outflowing nebula is coincident with the bright radio lobe seen in Figure 1. We will show that the majority of the emission-line gas is capable of being photoionized by the quasar’s ionizing radiation. However, the extremely high-velocity gas kinematics is possibly created due to the interaction of the radio jet with the environment.

The paper is organized as follows: Section 2 outlines the JWST NIRSpec data used in this study and the associated data reduction steps. Section 3 discusses the kinematic analyses performed on the reduced data cubes. The subsequent results are narrated in Section 4. In Section 5, we discuss the implications of the results and end with the conclusion in Section 6.

Throughout this paper, we assume a flat cosmological model with  $H_0 = 70 \text{ km s}^{-1} \text{ Mpc}^{-1}$ ,  $\Omega_m = 0.30$ , and  $\Omega_{\Lambda} = 0.70$ , and all magnitudes are given in the AB magnitude system (Oke & Gunn 1983).

## 2. Observations

### 2.1. NIRSpec Integral Field Unit Observations

The JWST/NIRSpec observations of TNJ1338 reported here were taken as part of the Cycle 1 GO program 1964 (PIs: Overzier and Saxena) on 2023 February 22 beginning at 22:43:58 UTC, using two grating-filter combinations: G235H/F170LP and G395H/F290LP. All the JWST data used in this paper can be found in MAST doi:10.17909/v0kq-8381. The



NIRSpec IFU provides spatially resolved spectroscopy over a  $3'' \times 3''$  field of view with  $0.''1 \times 0.''1$  spatial elements. The observations were taken with an NRSIRS2 readout pattern and 16 groups per integration, with a total of two integrations in a four-point dither pattern. An on-source integration time of  $\sim 9.5$  ks was used for each grating, with a total on-source exposure time of 18,680 s. An equal integration time was spent to nod off scene for good-quality background subtraction. The source was acquired using available deep HST and high-resolution VLA radio imaging. The resultant spectra cube has spectral resolution  $R \sim 2700$ , over the wavelength range 1.66–5.27  $\mu\text{m}$  (rest-frame 3200 to 10300 Å). For a full description of the data acquisition and reduction, we refer the reader to Saxena et al. (2024). Below we summarize briefly the key steps of the data reduction.

## 2.2. NIRSpec Data Reduction

All the analyses and reduced data cubes presented in this paper are based on the Space Telescope JWST pipeline version 1.11.1 (Bushouse et al. 2023), and the context file `jwst_1118.pmap`. This latest calibration reference file incorporates proper in-orbit flat-fielding and improved flux calibrations. All the individual raw images are first processed for detector-level corrections using the `Detector1Pipe-line` module of the pipeline (Stage 1). The input to this stage is raw nondestructively read ramps. A number of detector-level corrections are performed in this stage such as data quality and saturation check, dark current subtraction, superbias subtraction, fitting ramps of nondestructive group readouts, linearity, and persistence correction. The output is uncalibrated count-rate images per exposure per integration.

The resultant images are then processed with `CALWEBB_SPEC2`, Stage 2 of the pipeline. This step assigns a world coordinate system to each frame, flags pixels affected by Micro-Shutter Assembly (MSA) “failed” open shutters, and performs flat-field correction. An image-from-image background subtraction is performed using the observations of the dedicated off-scene background. Finally, flux calibrations are performed with the most updated in-flight calibrations to convert the data from count rates to flux density in cgs units. We skip the imprint subtraction step since it increases the overall noise level in the final data cube. The individual Stage 2 images are resampled and coadded in the final Stage 3 of the pipeline (`CALWEBB_SPEC3`). Before combining the individual data cubes, an outlier-detection step is required to identify and flag cosmic rays and other artifacts in the reduced data. However, the “outlier-detection” step in the pipeline tends to identify an excess of false positives and occasionally marks strong emission lines as outliers. We therefore skip the default algorithm and use our custom routine that determines outliers across the different dither positions. We utilize a sigma-clipping technique to remove the outliers. We additionally used python package `astroscrappy` (McCully et al. 2018), which is a python version of the widely used `LACosmic` routine (van Dokkum 2001), to remove any other residual outliers missed by the sigma-clipping technique. We mask the outliers and exclude them from the data sets. The cleaned dithered observations are assembled to create the final 3D data cube using the `cube_build` step. We select the exponential modified Shepard method (“`emsm`”) of weighting when combining detector pixel fluxes to provide high a signal-to-noise ratio (S/N) at the spaxel level. The data cube is produced with a spaxel size of  $0.''1$ .

The uncertainty in NIRSpec IFU astrometry can be anywhere between  $\sim 0.''1$ – $0.''3$ . There is a spatial offset between the astrometry of the NIRSpec IFU obtained from this program (GO 1964) and the NIRCAM images of TNJ1338 obtained from the PEARLS collaboration (GTOs 1176 and 2738; Duncan et al. 2023) by  $\sim 0.''1$ . This is likely dominated by the pointing uncertainty of the IFU mode. The NIRCAM mosaics are matched with Gaia Data Release 3 (after applying proper motion corrections) and are much more accurate, with an uncertainty level of  $\pm 0.''02$ . Hence, we reregister our NIRSpec IFU maps by aligning the continuum map obtained from our NIRSpec observations (shown later in Figure 3, top left panel) with the NIRCAM/F300M-derived continuum image. Thus, the spatial alignment between our NIRSpec maps and the VLA radio continuum images (presented in Figure 1, and shown later in Figures 3–6) has an associated uncertainty  $\pm 0.''02$ .

## 3. Data Analyses

Spatially resolved rest-frame optical emission lines are obtained with the JWST NIRSpec IFU spectroscopy for TNJ1338. The data reduction pipeline steps, outlined in Section 2.2, produce wavelength and flux-calibrated, combined, and rectified spectra for each spaxel in a three-dimensional data cube. Figure 2 shows the spectra taken with the G235H grating, extracted within the host (H) and the nebular (N) apertures, as marked in Figure 1. These spectra were obtained by summing the spectra from the spatial pixels lying within the respective apertures where the S/N of the [O III] 5007 Å line exceeded  $3\sigma$ . Multiple emission lines are detected, including [O III] 4959 Å, [O III] 5007 Å, [O II] 3727, 3729 Å, H $\beta$ , [Ne III] 3868 Å, and [Ne V] 3435 Å, and many others in the G395H grating (H $\alpha$  + [N II] 6584 Å and [S II] 6717, 6731 Å).

We derive the systemic redshift,  $z = 4.104 \pm 0.001$ , from the measured wavelength of the integrated [O III] 5007 Å emission extracted within the host galaxy (H marked in Figure 1) as shown in Figure 2. This is roughly in agreement with the previously reported value of  $z = 4.1057 \pm 0.0004$ , based on the He II emission line from MUSE rest-frame ultraviolet (UV) spectra (Swinbank et al. 2015). The discrepancies of  $\sim 450$  km  $\text{s}^{-1}$  possibly arise because the flux-weighted center of the He II line used by Swinbank et al. (2015) could be significantly offset from that of the host position. Besides, the presence of chaotic kinematics and powerful outflows can affect all the prominent rest-frame UV to near-infrared emission lines. Moreover, [O III] is a more reliable estimator of the systemic redshift than rest-frame UV lines. Thus in our study, all the emission lines are constrained to have our measured  $z = 4.104$ .

Our analyses are primarily based on emission lines. So the first step is subtraction of the continuum level from the reduced data cubes per spaxel. To model the continuum emission around each emission line, we select spectral windows to that specific line’s immediate red and blue side. For our most widely used [O III] 5007 Å emission line, we select continuum windows at rest-frame 4900–4925 Å in the blue side and 5075–5100 Å in the red side. For the [O II] 3727, 3729 Å doublet, we select 3660–3680 Å and 3778–3880 Å, and for H $\beta$ , we choose 4820–4840 Å and 4880–4900 Å. These wavelength ranges are selected to be closest to the said line while ensuring that there is no contamination from any emission line. Next, we fit a second-order polynomial curve within the wavelength

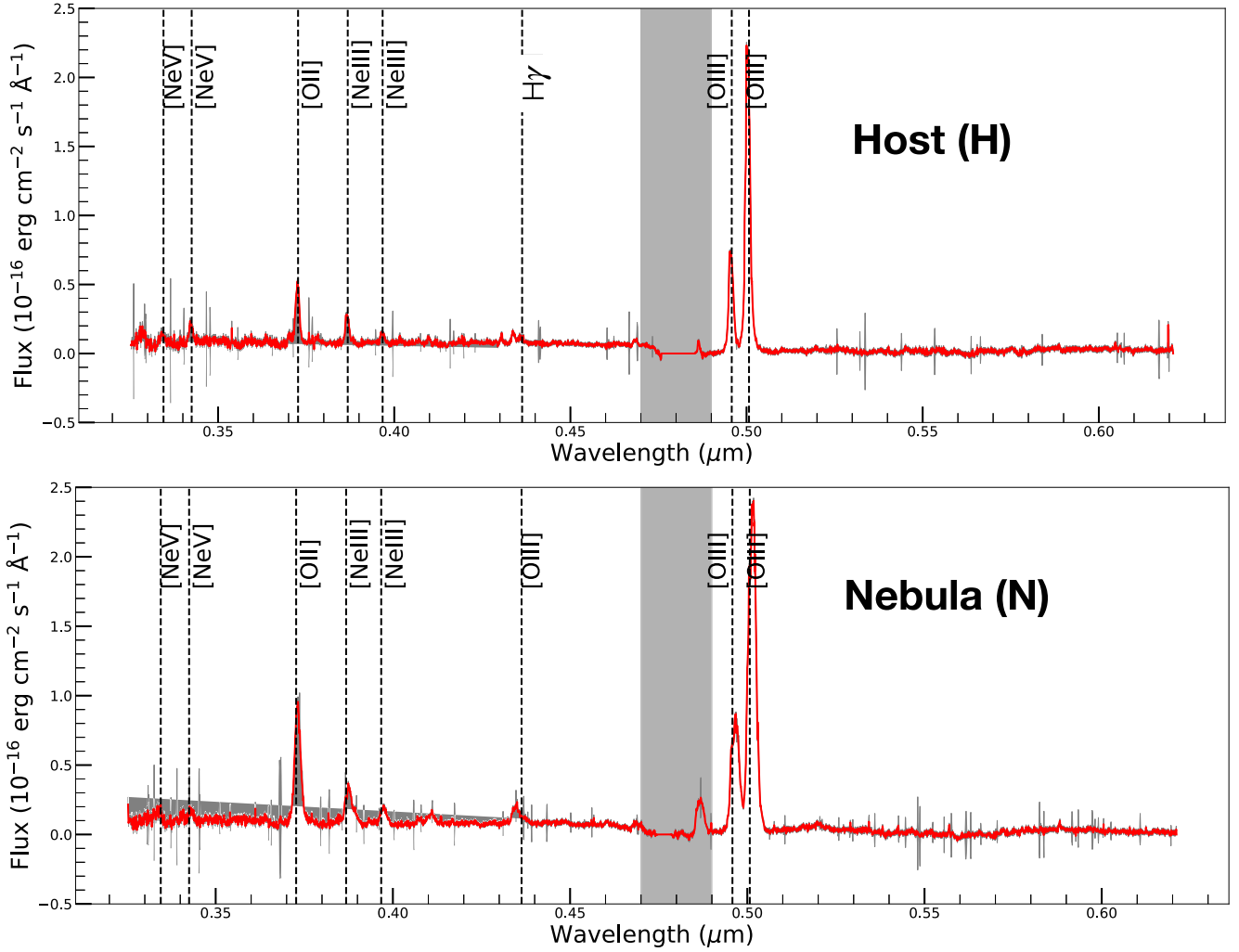


**Figure 2.** Top panel: the JWST/NIRSpec IFU spectra extracted from the host galaxy region (H) in the southern part of TNJ1338. The spectra shown are within a central circular aperture of radius 2 kpc for the blue wavelength channel. The gray-shaded region shows the  $1\sigma$  errors in the measured fluxes. The rest-frame optical nebular emission lines visible in the spectral window are marked by black dashed lines. Bottom panel: spectra extracted from the nebular-emission-line-dominated region (N), within a circle of radius 4 kpc. The circular apertures encompassing the H and N regions are marked in Figure 1.

range bounded by the above wavelength window using SCIPY’s least squares optimization module. The fitted continuum is subtracted from the emission-line spectra, and the process is repeated for every spaxel to create a continuum-subtracted emission-line cube. This method provides a robust subtraction of the continuum level for each line.

We constructed pseudo-narrow-band (NB) images for the detected emission lines using the continuum-subtracted NIRSpec data cube. The maps are centered on the position and wavelength of the corresponding line. We used a wide spatial aperture to include all the detectable emissions associated with TNJ1338, above the noise level. The spectral bandwidths for constructing the NB image were chosen to include more than 95% of the total integrated line flux and to maximize the S/N within a circular aperture of radius 2 kpc ( $0.''3$ ) centered on the host galaxy. The resulting continuum-subtracted NB images for seven different emission lines are shown in Figure 3.

We create moment 0 (intensity), moment 1 (velocity), and moment 2 (dispersion) maps from the [O III]  $\lambda 5007$  emission-line data cubes after the continuum level has been robustly subtracted out. Any spatial pixel with emission-line S/N  $< 2$  is masked out. This threshold is chosen to be able to capture the

faint emission structures while simultaneously discarding the noisy regions beyond our object of interest. We also nonparametrically calculate the different tracers of gas velocity dispersions—e.g., FWHM,  $W_{50}$ , and  $W_{80}$  (defined later)—for those two emission lines, without performing any model fitting. This enables us to directly extract the kinematics from the data and not make any assumption about the shape of the emission line (i.e., whether it is a Gaussian, Lorentzian, or Voigt profile).

$W_{50}$  is defined as the line width containing 50% of the emission-line flux, and  $W_{80}$  as the line width containing 80% of the emission-line flux. The  $W_{50}$  map of an emission line is calculated by computing the cumulative distribution function ( $\text{CDF}(x) = \text{P}(X \leq x)$ , which is the probability that the random variable  $X$  is less than or equal to  $x$ ) of the normalized line flux values for each spaxel. The velocity values corresponding to 25% ( $v_{25}$ ) and 75% ( $v_{75}$ ) of the integrated flux values are calculated from the CDF evaluated at  $x=0.25$  and  $0.75$ , respectively. Then,  $W_{50} = v_{75} - v_{25}$ . Similarly,  $W_{80}$  is calculated from the difference of  $v_{90}$  and  $v_{10}$ . We calculate the FWHM by finding half of the peak flux on either side of the line profile, and calculating the distance between those points.

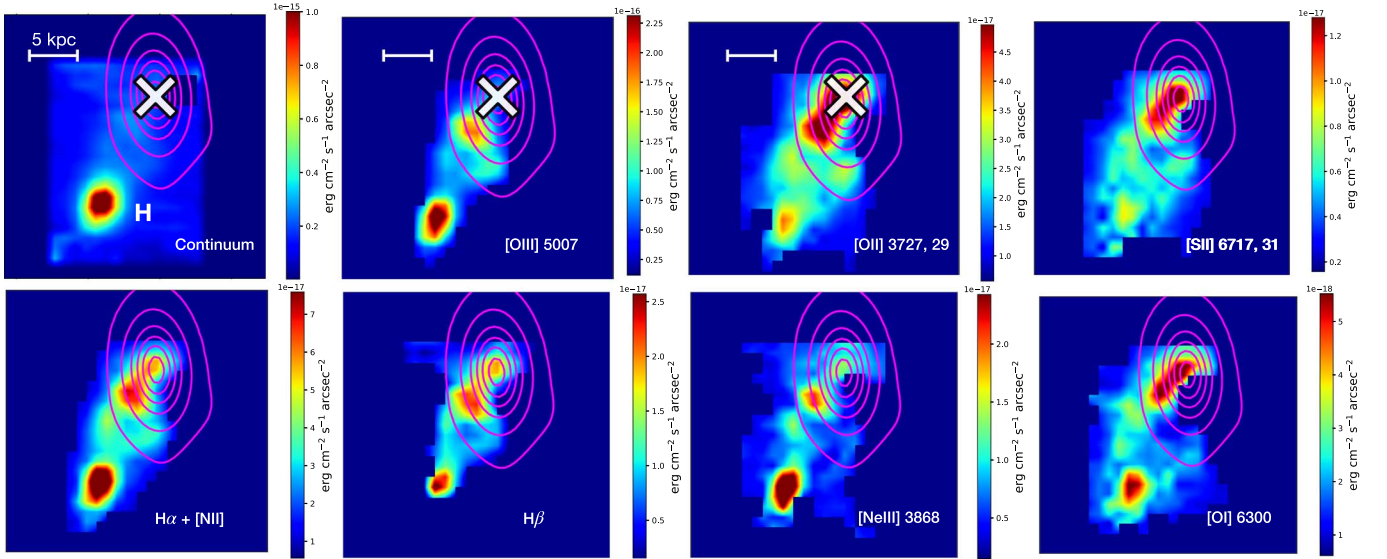


**Figure 3.** The first panel [top left] shows a continuum map, where all emission lines are masked. North is up. The host galaxy (H) in the southern end of TNJ1338 is indicated by a strong continuum presence. Line-integrated continuum-subtracted flux maps of [O III] 5007 Å, [O II] 3727, 3729 Å, [S II] 6717, 6731 Å, H $\alpha$  + [N II] 6584 Å, H $\beta$ , [Ne III] 3868 Å, and [O I] 6300 Å are shown in the remaining panels. The units of the maps are  $\text{erg cm}^{-2} \text{s}^{-1} \text{arcsec}^{-2}$ . The VLA radio image is overlotted on top in all the panels with magenta contours, with contours similar to Figure 1. The northern region is dominated by nebular (N) emission-line gas and exhibits diverse morphology in different line tracers. This extended emission region is spatially aligned (and roughly coincident) with the northern bright radio lobe (the center of the lobe is marked by a white cross).

## 4. Results

### 4.1. Emission-line Morphology

The morphology of the warm ionized gas in TNJ1338 traced by the different emission lines are shown via the pseudo-NB images in Figure 3. The VLA 4.5 GHz radio contour around the host galaxy and the northern radio lobe, with contours showing 1%, 10%, 30%, 50%, 70%, and 90% of the peak intensity similar to Figure 1, is overlotted on top in magenta. The emission maps of all the lines are very irregularly shaped and show extended nebulosities of ionized gas. In our companion paper (Saxena et al. 2024), we discuss the ionization structure and the detailed morphology and emission-line ratios of the different ionized gas tracers. The size of the extended ionized region is roughly  $\sim 15$  kpc along the major axis and  $\sim 7$  kpc in the perpendicular direction. The rest-frame optical continuum, shown on the first panel, is not contaminated by line emission. The continuum map is obtained by collapsing over the line-free wavelength region over the full available spectral bandwidth. TNJ1338 has a single, unresolved continuum source indicating the location of the host galaxy with an obscured quasar.

[O III] 5007 Å is the strongest emission line in our NIRSpc data cube, and thus the best tracer of ionized gas and outflows in our target TNJ1338. We will primarily focus on the [O III] emission in the rest of this section. Figure 3 (second panel) shows the continuum-subtracted NB [O III] image, produced by the method described in Section 3. Two distinct [O III]-bright regions are clearly visible. The peak in the [O III] surface brightness map coincides with the optical-continuum-bright region and hence indicates the emission from the host galaxy (marked as H in Figure 1) with an obscured quasar. However, nearly all the rest of the [O III]-line-emitting gas lying in the upper part of the map indicates a predominantly emission-line-dominated region (region N in Figure 1) with almost no detectable continuum with  $S/N > 5$ . This extended plume of [O III] is roughly aligned with the radio-jet axis and spatially

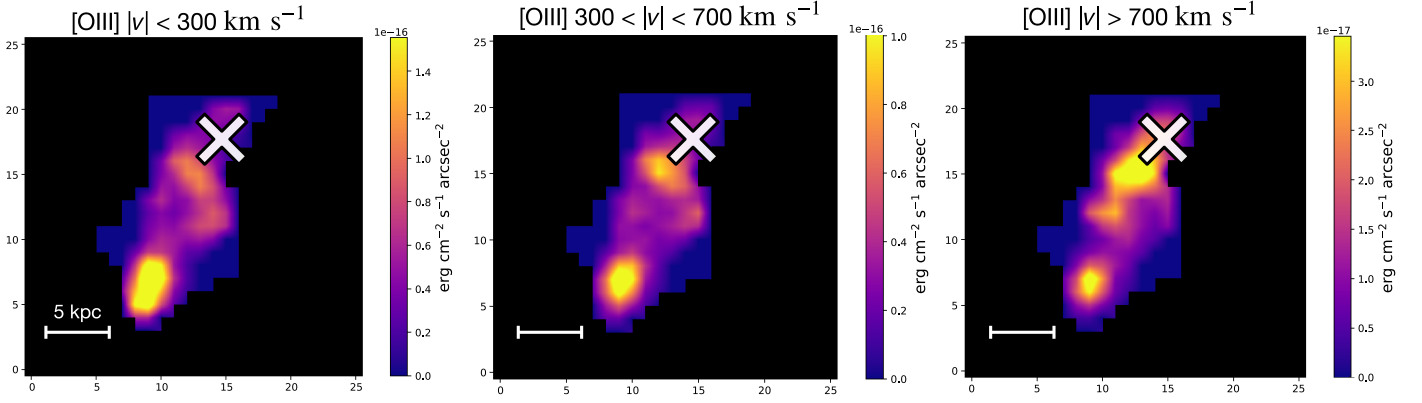
coincides with the bright northern radio lobe, shown with magenta contours in Figure 3. The position of the peak radio intensity, which indicates the approximate location of the radio lobe center, is shown using a white cross. The line emission extends to at least 12 kpc from the center of the host galaxy. The excellent angular resolution ( $\sim 0''.1$ ) and sensitivity of JWST NIRSpc reveal these intricate substructures within the ionized gas distribution.

As we will discuss in Section 4.2, the measured large velocities, increased line widths, and asymmetric line profiles measured in the extended ionized gas are clear outflow signatures. Their spatial coincidence with the radio lobe possibly indicates a scenario where the jet encounters dense gas and inflates a cocoon/bubble, which entrains gas clouds creating these observed outflows.

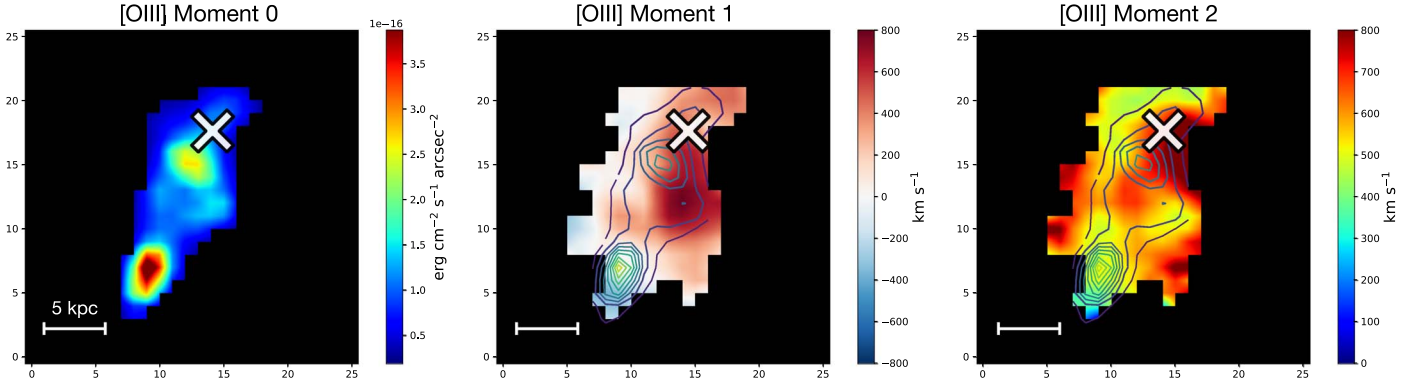
### 4.2. [O III] Kinematics

Figure 4 shows the [O III] 5007 Å emission maps in three different velocity channels:  $[-300, 300] \text{ km s}^{-1}$ ,  $[|300|, |700|] \text{ km s}^{-1}$  (which includes  $[-300, -700]$  and  $[300, 700] \text{ km s}^{-1}$ ), and  $[|700|, |1500|] \text{ km s}^{-1}$ .

We see similar patterns in the H $\alpha$  + [N II] and [O II] lines, but as mentioned before, we restrict our kinematic discussion primarily to [O III] 5007 Å emission since this is a bright forbidden line and is an ideal tracer of outflows. A collimated emission with a linear morphology is evident most prominently in the highest-velocity bin ( $|v| > 700 \text{ km s}^{-1}$ ). Indeed, the majority of the rapidly moving gas emission is located in the nebular-line-dominated region and is roughly coincident with the spatial location of the radio lobe detected in early VLA data. The [O III] emission in this velocity bin is peaking at a projected distance of  $\sim 9$  kpc from the peak of the continuum emission from the host galaxy. The velocities we measure in this region exceed  $1000 \text{ km s}^{-1}$  and are well in excess of gas undergoing rotational motion under the influence of gravity. This morphology clearly confirms a fast-moving outflow, as



**Figure 4.** Velocity channel maps for the [O III] 5007 Å line emission. The left panel shows the [O III] line flux with velocities within  $\pm 300 \text{ km s}^{-1}$  around the systemic velocity ( $v_{\text{sys}}$ ), thus highlighting the slowest-moving ionized gas. The middle panel shows the intermediate-velocity components and the right panel highlights the fastest-moving part of the ionized wind with  $v > +700 \text{ km s}^{-1}$  and  $v < -700 \text{ km s}^{-1}$ . The white cross shows the spatial position of the bright radio lobe from the VLA image. Clearly, the fastest-moving gas coincides with the nebular region where the bright radio lobe lies. We hypothesize that an expanding cocoon driven by the shocked jet fluid accelerates the ambient gas outwards to large velocities (see Section 5.3).



**Figure 5.** Moment 0 [left panel], moment 1 [middle panel], and moment 2 [right panel] maps of the [O III] 5007 Å line emission of TNJ1338. The black contours indicate the [O III] moment 0 contours and the white cross marks the position of the northern radio lobe. The host galaxy exhibits an intermediate velocity ( $|v| \sim 400 \text{ km s}^{-1}$ ), while the nebular region exhibits velocity exceeding  $1000 \text{ km s}^{-1}$ . The moment 2 values are very high in the spatial locations coincident with the radio lobe, indicating broad line widths ( $\sigma > 1000 \text{ km s}^{-1}$ ) and turbulent motions in the ambient medium where the bow shock is generated at the terminus of the jet. See Section 5.3 for a more detailed discussion.

previously hinted in De Breuck et al. (1999) and Swinbank et al. (2015). We also detect some high-velocity gas within the inner few kiloparsecs of the central region of the host galaxy. This can be driven by the central quasar. However, in this work, we mostly focus on the large-scale outflow in the nebular [O III]-dominated region.

As we move to the lower velocity bins ( $|v| = 300$  to  $700 \text{ km s}^{-1}$ ), a remarkable change in the [O III] morphology is apparent. The brightest emission in this velocity range now peaks at the host galaxy centered on the continuum, but a filament of line emission becomes evident at the [O III]-emitting region, extending perpendicular to the fastest-moving [O III] outflow probed in the highest-velocity bin. This intermediate-velocity emission seems to connect the lowest-velocity [O III] ( $|v| < 300 \text{ km s}^{-1}$ ) centered on the host galaxy to the high-velocity outflowing gas lying coincident with the radio lobe.

The kinematics maps in Figure 5 also strongly highlight the features we discussed above. This figure shows the moment 0, moment 1, and moment 2 maps of the total [O III]  $\lambda 5007$  emission with moment 0 contours overplotted on top. The moment 1 map shows that the highest-velocity offset from the systemic, i.e.,  $v > 1000 \text{ km s}^{-1}$ , is indeed exhibited by the emission-line-dominated region associated with the northern radio lobe (shown by white cross). The host galaxy region

shows an absolute velocity offset lower than  $400 \text{ km s}^{-1}$ . The fainter, filamentary structure with intermediate velocity ( $300 < |v| < 700 \text{ km s}^{-1}$ ) connects the host galaxy AGN with the outflow region. The absolute moment 1 values depends on the exact determination of the zero-point, or redshift of the system. We derive the redshift from the measured [O III] velocity at the central stellar continuum peak. The presence of blueshifted and redshifted velocity components indicates a laterally expanding bubble/cocoon of emission-line gas, possibly driven by the shocked radio jet, which may accelerate gas outwards in radial directions. See later in Section 5.3 for a more detailed discussion of the jet-driven feedback scenario.

These large velocity values and the distinct gas morphology at different velocity channels are incompatible with the rotational motion associated with the host galaxy. We also see an extremely high gas dispersion exceeding  $1200 \text{ km s}^{-1}$  coincident with the [O III]-emitting gas associated with the largest velocity. Figure 6 shows a nonparametric characterization of the width of the emission lines, measured using the process discussed in Section 3, and shows very similar results. We show  $W_{50}$ ,  $W_{80}$ , and FWHM for the [O III] 5007 Å line. The maximal line width is not associated with the central regions of the host, as probed by the position of the continuum peak. Using all three tracers of emission-line widths, we find



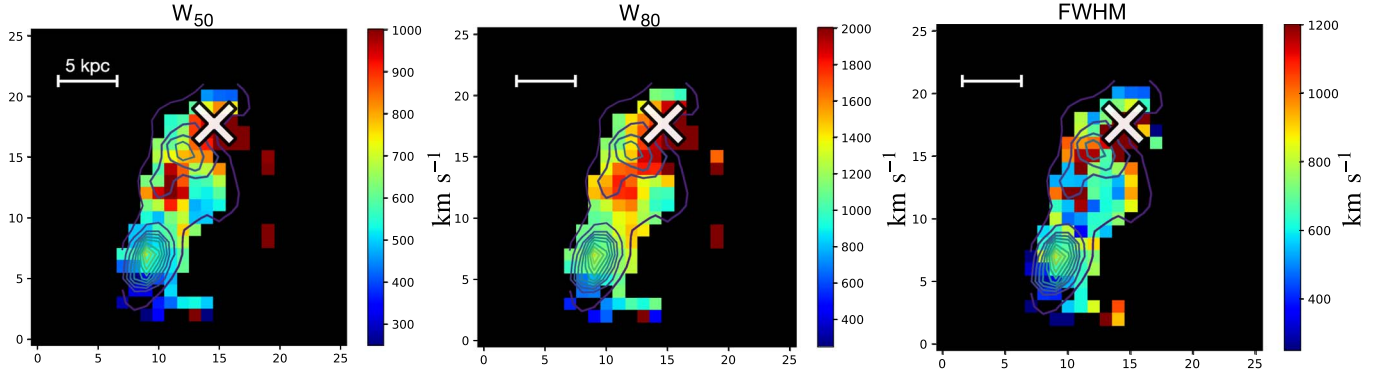


**Figure 6.** Different kinematic tracers (line widths) of the [O III] line emission. Left panel: map of  $W_{50} = v_{75} - v_{25}$ , which is the line width containing 50% of the emission-line flux. Here  $v_{75}$  and  $v_{25}$  are velocities at the 75th and 25th percentiles of the overall emission-line profile in each spaxel. Middle panel: map of  $W_{80}$ , where  $W_{80} = v_{90} - v_{10}$ . Right panel: FWHMs of the [O III] line profiles. Solid contours in all three panels show [O III] flux, and the white cross indicates the center of the bright radio lobe. Broad line widths are prevalent in the emission-line-dominated nebular region (marked as N in Figure 1), coincident with the radio lobe.

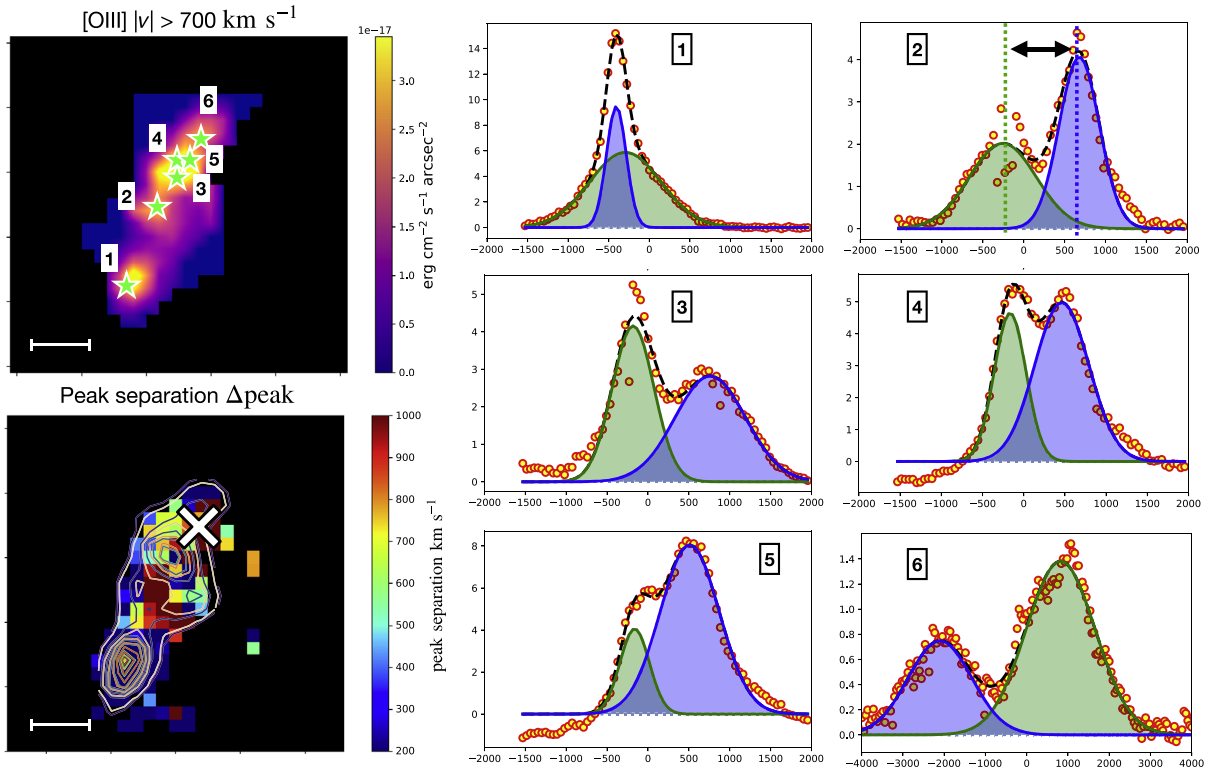


**Figure 7.** Top left: a channel map for the [O III] 5007 Å line, with  $|v| > 700 \text{ km s}^{-1}$ . Right panel: emission-line profile around the [O III] 5007 Å emission line shown for six different spatial positions, marked by green stars in the top left panel. The line profiles indicate multicomponent velocity profiles, with broad lines and extended “winged” line shapes. The emission-line profiles become more kinematically complex as we approach the nebular region, close to the radio lobe, and they have a greater peak-to-peak separation. Bottom left: a resolved map of the peak-to-peak separation ( $\Delta_{\text{peak}}$ ) of the [O III] line profiles extracted from each spaxel, by fitting the line profiles with two components. The white cross indicates the spatial location of the bright radio lobe, as before.  $\Delta_{\text{peak}}$  exceeds  $1000 \text{ km s}^{-1}$  in the northern nebular region, consistent with Figures 5 and 6.

extremely broad line widths ( $W_{50} > 1200 \text{ km s}^{-1}$ ,  $W_{80} > 2000 \text{ km s}^{-1}$ ) spatially associated with the northern radio lobe, consistent with the velocity dispersion map. The increased line widths provide clear evidence that the extreme gas kinematics must be an outflow. The spatial coincidence with the radio lobe implies that this is likely a signature of a jet-driven outflow. The host galaxy shows a moderate line width with a mean  $\text{FWHM}_{\text{avg}} \sim 800 \text{ km s}^{-1}$  within the central  $0''.5$  around the peak of the stellar continuum. This is consistent with our interpretation from the highest-velocity channel maps in Figure 5 that the upper [O III]-enhanced region must be associated with high-velocity outflowing gas clouds.

In Figure 7, we show the [O III] 5007 Å spectral profiles at six spatial locations (aperture size =  $0''.1$ ) along the straight line connecting the host galaxy and the high-velocity outflow region. Although the host galaxy also shows a clear signature of a broad outflow component in the line profile, the spectral components become broader as we move toward the emission-line-dominated region. There are two distinct components clearly visible with each component having  $\text{FWHM} > 700 \text{ km s}^{-1}$ . We avoid spectral fitting throughout our analyses, because of these extremely broad spectral profiles where deblending into different components becomes very uncertain due to parameter degeneracy. However, in this step, we want to



extract the peak-to-peak separation between the two distinct components. Hence, we fit the spectral profiles using two Gaussian components to extract the location of the two peaks, without worrying about the exact number of kinematic components needed to optimally fit the spectra. We plot the peak separation ( $v_{\text{sep}}$ ) and find that  $v_{\text{sep}}$  also exceeds  $1200 \text{ km s}^{-1}$  in agreement with the  $W_{50}$  and FWHM estimates. Thus, to summarize, we identify:

1. A bright [O III]-emitting region with a high-velocity offset ( $|v| > 700 \text{ km s}^{-1}$ ) and broad line width (FWHM  $> 1200 \text{ km s}^{-1}$ ) with a bubble-like morphology. This kinematic component is centered at a projected separation of  $\sim 0''.9$  from the center of the host galaxy's continuum emission. This fast-moving component spatially coincides with the brighter radio lobe of the central radio galaxy and indicates a jet-driven outflow scenario.
2. A region with comparatively narrow (FWHM  $\sim 700 \text{ km s}^{-1}$ ) emission lines centered close to the systemic velocity ( $|v| < 300 \text{ km s}^{-1}$ ). This is associated with the host galaxy which harbors a central obscured quasar.
3. A region with intermediate-velocity offsets ( $300 < |v| < 700 \text{ km s}^{-1}$ ) and line widths ( $600 < \text{FWHM} < 1000 \text{ km s}^{-1}$ ) connecting the host galaxy center with the outflow.

Similar broad and fast-moving gas is detected in other strong emission lines as well, particularly  $\text{H}\alpha$ , [O II], [N II], and [S II]. As shown in the NB images in Figure 3, bright, linear, extended emission is indeed coincident with the radio lobe (white cross) observed at the outflowing region in all the emission maps, very similar to the [O III] emission, albeit with some small-scale structural differences. We leave the detailed analyses of the kinematics of the other strong emission lines and the similarities between each other for future work.

#### 4.3. Outflow Rates and Energetics

In the previous section, we presented clear detection of fast-outflowing gas, traced by the broad [O III]  $\lambda 5007$  emission lines (FWHM  $> 700 \text{ km s}^{-1}$  in Figure 6) and high-velocity offset ( $|v| > 1000 \text{ km s}^{-1}$ ) across a large part of our target galaxy TNJ1338. In this section, we will study the spatial distribution of the mass of the outflowing gas, outflow rates, and the associated energetics of the warm ( $T \sim 10^4 \text{ K}$ ) ionized gas. The extremely high spatial resolution ( $\sim 0''.1$ ) and sensitivity of the JWST/NIRSpec IFU data presented here enable a detailed investigation of the ionized outflow rates and energetics across the entire galaxy. We note that this is the first time such a high-resolution characterization of a jet-driven outflow has been done in a  $z > 4$  radio galaxy hosting an obscured quasar. Previous IFU studies at similar redshifts (Nesvadba et al. 2017) used ground-based data with an angular resolution of  $\sim 0''.5$  to  $1''$ . There have been several other ground-based resolved studies of extended outflow in HZRGs (van Ojik et al. 1997; Villar-Martín et al. 2003; Humphrey et al. 2007), but the lack of sufficient angular resolution has affected the energetics measurements. The majority of the studies have relied on spatially unresolved information and the detection of broad absorption features of UV resonant lines (Wang et al. 2018; Onoue et al. 2019; Bischetti et al. 2022, 2023). These features primarily trace nuclear outflows which encompass a small fraction of the galactic-scale outflow. Moreover, the absence of spatial information prevents a reliable estimate of the outflow parameters. In the section below, we outline how we estimate the mass, outflow rate, and

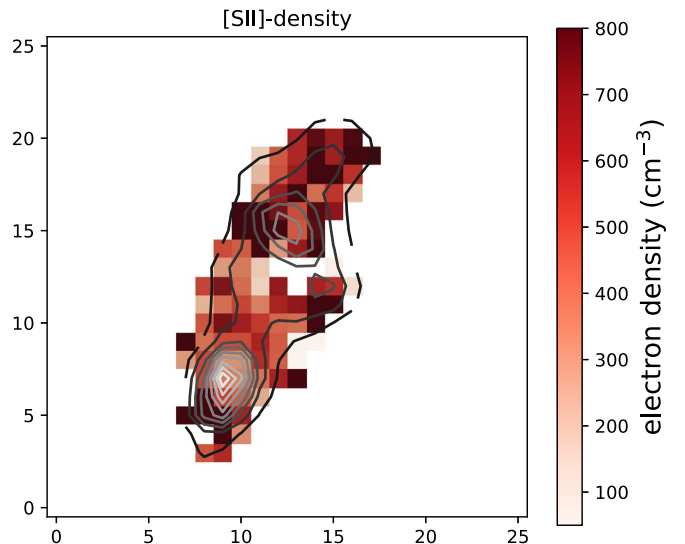


**Figure 8.** Electron density map of TNJ1338, derived using the line ratios of the [S II]  $\lambda\lambda 6717, 6731 \text{ \AA}$  doublet ratio (see Section 4.3). The solid contours represent the [O III] emission flux. X and Y indicate spatial pixels. The density ranges from  $200\text{--}1000 \text{ cm}^{-3}$ , with mean values of  $570 \text{ cm}^{-3}$  and  $610 \text{ cm}^{-3}$  in the host and nebular region, respectively (see Table 2).

energetics of the ionized outflow, and discuss the potential mechanisms responsible for driving the galaxy-scale outflow.

The first step is an accurate measurement of electron density  $n_e$  and its spatial variation at various locations within the galaxy. We derive  $n_e$  using the [S II]  $\lambda\lambda 6717, 6730$  line ratio. Each of the two [S II] lines was fitted using a two-component Gaussian for every spaxel, and the two components are tied together by the same velocity and dispersion value obtained from the brighter [O III]  $\lambda 5007$  moment 1 and 2 maps. This step is necessary to ensure accurate density measurements by extracting the line ratios properly. We wrap the fitting module into the python package *dynesty* (Speagle 2020; Kozlov et al. 2022), which uses a dynamic nested sampling algorithm (Skilling 2004, 2006) to execute a multiparameter optimization and extract Bayesian posteriors and evidence. Although there might still be unaccounted uncertainty owing to the simple double-Gaussian model we fit, we strictly avoid overfitting the complex line profiles. We used the total [S II]  $\lambda\lambda 6716, 6730$  lines flux, the parameterization of Sanders et al. (2016), and the assumption of  $T_e = 10^4 \text{ K}$  to convert to electron density. In Figure 8, we show the resulting electron density map. The density varies between  $200\text{--}1100 \text{ cm}^{-3}$ , and the nebular-emission-dominated region with the fast outflow signatures shows the highest values of the density. This is consistent with other local and high- $z$  AGN studies, which have found higher density estimates in the outflow component compared to the rotating disks in the host galaxy (Villar Martín et al. 2014; Mingozzi et al. 2019; Cresci et al. 2023).

Next, we calculate the Balmer decrement, i.e.,  $\text{H}\alpha/\text{H}\beta$  as shown in Figure 9, which is a direct probe of dust extinction. Indeed, the host galaxy of TNJ1338 harbors an obscured quasar in the center and is thus expected to be dust enshrouded with a higher  $\text{H}\alpha/\text{H}\beta$  ratio. We indeed find that the average  $\text{H}\alpha/\text{H}\beta$  is the highest in the central region of the host galaxy, with a median value  $= 4.29 \pm 1.1$ . For the extended gas, the ratio goes down to  $3.1 \pm 0.8$ . The extinction estimates are derived from the measured Balmer decrement, assuming a standard  $R_V = 3.1$  extinction curve (Osterbrock & Ferland 2006) and the temperature of the ionized gas to be  $\sim 10^4 \text{ K}$ . The mean

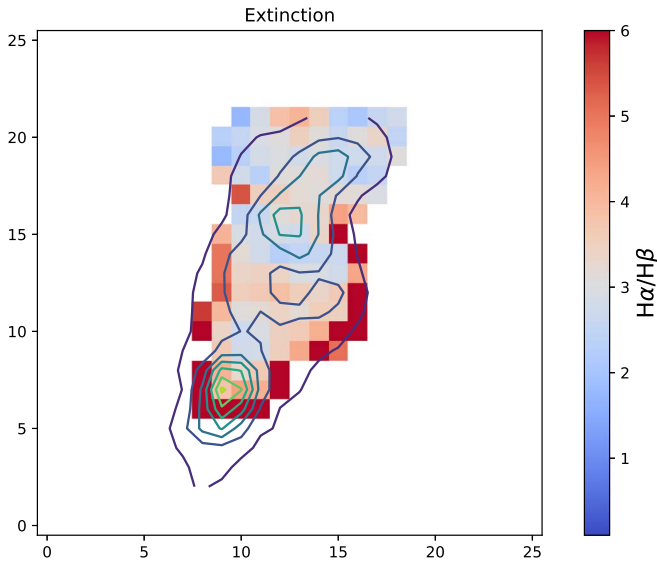


**Figure 9.** Balmer decrement measurement, i.e.,  $H\alpha/H\beta$  emission-line ratios, with the [O III]  $\lambda 5007$  flux overplotted as contours. X and Y indicate spatial pixels. These measurements are used for dust correcting the [O III] luminosities to compute the ionized gas mass and outflow rates.  $H\alpha/H\beta$  ratio spans from 7.11 in the host galaxy to 3.53 in the nebular region.

extinction measured  $A_V = 0.8$ . We perform dust correction for the emission-line fluxes before computing the outflow rates and energetics.

In this work, we have discussed large-scale outflow signatures using the [O III]  $\lambda 5007$  flux distribution, velocity, and line widths. The [O III]  $\lambda 5007$  emission line is the brightest line emitted by the outflow within the rest-frame visible range covered by the NIRSpc data cube. It is also well separated in wavelength from neighboring emission lines. Hence, we use dust-corrected [O III]  $\lambda 5007$  to calculate the ionized gas mass and energetics using the formula below (Cano-Díaz et al. 2012; Veilleux et al. 2020, 2023):

$$M_{\text{ionized}} = 5.3 \times 10^8 \frac{C_e L_{44}([\text{OIII}]\lambda 5007)}{n_{e,2} 10^{[\text{O}/\text{H}]}} M_{\odot}, \quad (1)$$

where  $L_{44}([\text{O III}]\lambda 5007)$  is the luminosity of [O III]  $\lambda 5007$ , normalized to  $10^{44} \text{ erg s}^{-1}$ ,  $n_{e,2}$  is the electron density normalized to  $10^2 \text{ cm}^{-3}$ ,  $C_e$  is the electron density clumping factor, which can be assumed to be of order unity, and  $10^{[\text{O}/\text{H}]}$  is the oxygen-to-hydrogen abundance ratio relative to solar abundance. We assume solar abundance, so  $[\text{O}/\text{H}] = 0$ , and thus  $10^{[\text{O}/\text{H}]}$  is 1. We use the spatially resolved density values derived from the [S II]  $\lambda\lambda 6716, 6731$  flux ratio as shown in Figure 8. The median electron density  $n_e = 570 \text{ cm}^{-3}$ , but it goes up to  $\sim 1150 \text{ cm}^{-3}$  in the outflowing regions. We use [O III]  $\lambda 5007$  line fluxes corresponding to the velocity channel  $|v| > 500 \text{ km s}^{-1}$  to include only the outflowing gas component that is well in excess of the observed velocities due to orbital motions (the maximum velocity consistent with orbital motion due to gravitationally bound orbits for TNJ1338 is  $\sim 250 \text{ km s}^{-1}$ ). We corrected this flux for extinction using the  $H\alpha/H\beta$  line ratio (see Figure 9) and converted it to luminosity, which yielded a total luminosity  $L_{[\text{O III}],\text{corr}} = 5.6 \times 10^{45} \text{ erg s}^{-1}$ . Note, for some of the spaxels, the  $H\beta$  emission line falls in the detector chip gap. The dust correction for those spaxels are made by taking the median  $H\alpha/H\beta$  line ratio, centered on the

host galaxy. In Figure 10 (upper left panel), we show the distribution of ionized gas obtained associated with the outflowing component. The extinction-corrected ionized mass surface density ranges from  $2 \times 10^7 - 5 \times 10^7 M_{\odot}$  per spatial pixel, with a total outflowing mass  $M_{\text{ionized}} = 4.8 \times 10^9 M_{\odot}$  (Table 1). The amount of ionized gas mass in the host versus the nebular region is tabulated in Table 2.

An estimate of the ionized gas mass can also be derived using the outflow component of the  $H\beta$  or  $H\alpha$  recombination line (Cresci et al. 2023; Marshall et al. 2023; Perna et al. 2023). Following this, we also measured the dust-corrected  $H\beta$  emission from the outflow, which yielded a total outflowing mass  $M_{\text{ionized},H\beta} = 3.8 \times 10^9 M_{\odot}$ . This is consistent with what we obtain from [O III]  $5007 \text{ \AA}$ . However, we note here that for a handful of spatial pixels, the  $H\beta$  emission line fell onto the NIRSpc detector chip gap and thus returned no value. Hence the calculated  $M_{\text{ionized},H\beta}$  is a lower limit. We return to the [O III]  $5007 \text{ \AA}$  derived mass estimate for the outflow mass rate and energetics calculation described below.

Once the outflow mass is inferred, the spatially resolved ionized outflow rate for each parcel of gas within the outflowing regions of TNJ1338 can be calculated using the following equation:

$$\dot{M}_{\text{out}} = \frac{M_{\text{out}} v_{\text{out}}}{R_{\text{out}}}. \quad (2)$$

Here we assume that  $M_{\text{out}}$  is the ionized gas mass surface density, i.e., the mass in each spatial pixel, as derived from Equation (1). We presume that each of these gas parcels with mass  $M_{\text{out}}$  is at a projected radial distance  $R_{\text{out}}$  from the host galaxy center, defined by the peak of the stellar continuum. We take the velocity in each pixel  $v_{\text{out}} = \sqrt{W_{50}^2 + \Delta v^2}$ , where  $W_{50}$  is the line width corresponding to 50% of the emission-line flux (see Section 4.2 for details), and  $\Delta v$  corresponds to the velocity offset from the systemic velocity. We obtain a total mass outflow rate  $\dot{M}_{\text{out}} = 497 \pm 47 M_{\odot} \text{ yr}^{-1}$ , and the spatially resolved mass outflow rate map is shown in Figure 10 (upper right panel). This large amount of outflowing gas makes this source stand out as one of the earliest known radio galaxies with the strongest outflow signature. The corresponding kinetic power of the outflow is given by:

$$\text{KE}_{\text{outflow}} = \frac{1}{2} \times \dot{M}_{\text{out}} v_{\text{out}}^2. \quad (3)$$

We obtained a total kinetic power of the emission lines gas to be  $1.01 \times 10^{44} \text{ erg s}^{-1}$ , and the total momentum rate of the outflow is  $\dot{p}_{\text{kin}} = \dot{M}_{\text{out}} v_{\text{out}} = 2.06 \times 10^{36} \text{ dyne}$ . The resolved maps of these quantities are shown in Figure 10 (bottom row), and their values in the host galaxy H and the nebular region N are mentioned in Table 1. The detailed implications of these findings are discussed in Section 5.

It is important to consider the impact of projection effects on these estimates. These will affect both  $v_{\text{out}}$  and  $R_{\text{out}}$ . The morphology and kinematics of the gas in the northern nebular region imply that both the structure of the gas and its outflow direction are aligned with the axis of the radio jet. Let us then designate the angle between the radio-jet axis and our line of sight as  $\phi$ . In this case the true value ( $v_{\text{out,t}}$ ) of the outflow velocity versus the projected value ( $v_{\text{out,p}}$ ) along our line of sight is  $v_{\text{out,t}} = v_{\text{out,p}} / \cos\phi$ , and the actual distance of the material from the nucleus versus the projected distance is given by

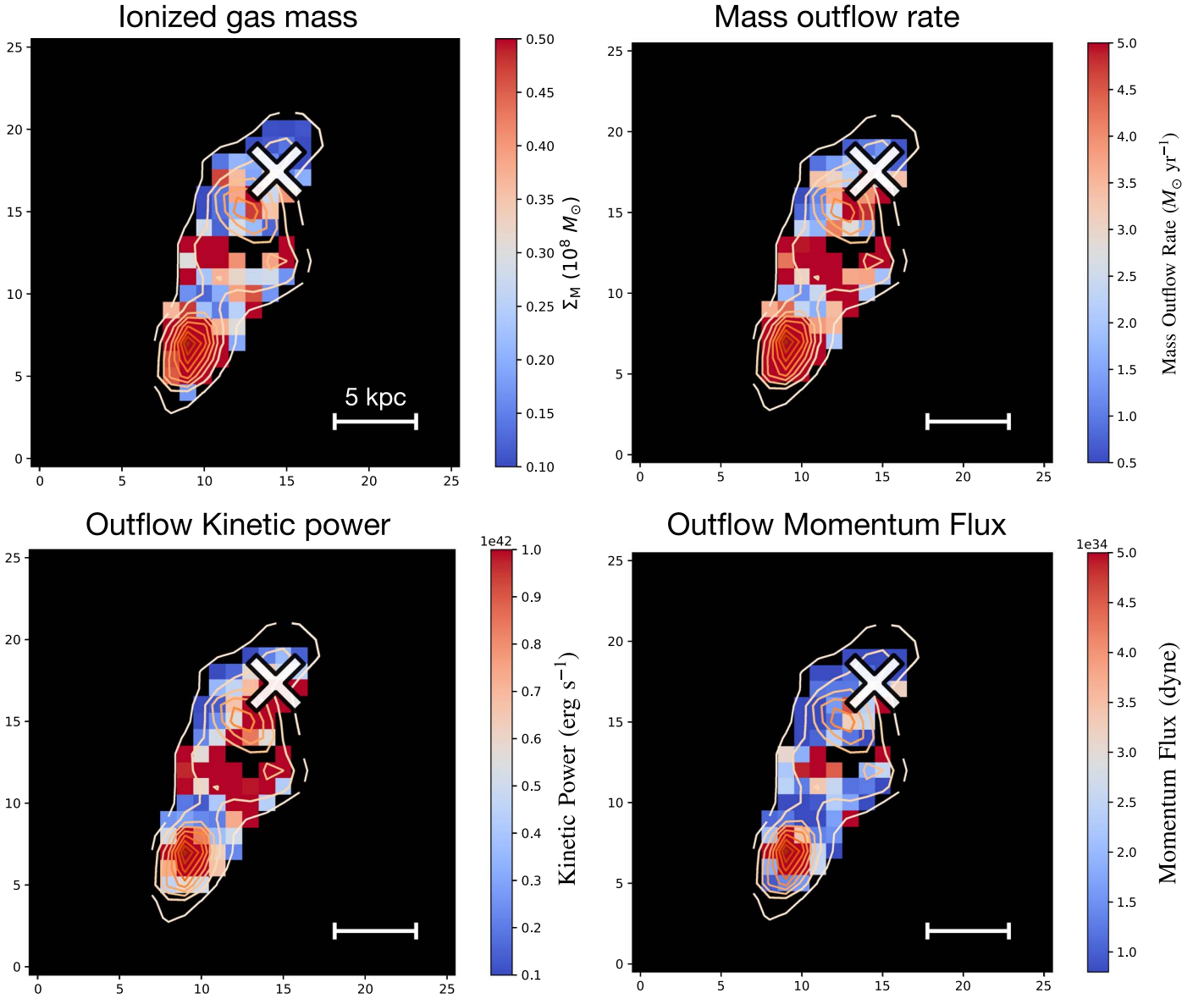


**Figure 10.** Top left: spatially resolved map of ionized gas mass surface density, in units of  $10^8 M_\odot$  per spaxel. The ionized gas mass is derived from the extinction-corrected [O III] luminosity and the [S II]-derived electron density (Equation (1)). The total ionized gas mass integrated over the whole galaxy is  $4.8 \times 10^9 M_\odot$  (Table 1). The solid contours represent [O III] 5007 Å emission flux and the white cross shows the location of the bright radio lobe. Top right: resolved map of ionized gas mass outflow rate, in units of  $M_\odot \text{ yr}^{-1}$ . The mass outflow rates are enhanced in discrete locations in both the host and the nebular regions, but with comparative values when integrated over spatial apertures marked as H and N ( $234 M_\odot \text{ yr}^{-1}$  and  $264 M_\odot \text{ yr}^{-1}$ ; Table 2). Bottom left and bottom right: outflow kinetic power and momentum rate in units of  $\text{erg s}^{-1}$  and dyne, respectively. The total kinetic power of the outflow  $\text{KE}_{\text{outflow}} \sim 10^{44} \text{ erg s}^{-1}$ , which is a small fraction of the kinetic power of the radio jet (Table 1), implying that the transfer of the kinetic power from the jet to the gas is not very efficient. See the detailed discussion in Section 5.3.

$R_t = R_p / \sin \phi$ . From this is clear that the above calculations of the total kinetic energy and momentum in the gas will be strict lower limits. Since we do not know  $\phi$  we will just assume its median value of  $60^\circ$  (that is, half of  $4\pi$  lies in the region with  $\phi < 60^\circ$ ). In this case, the median value for  $v_{\text{out,t}}$  would be  $2v_{\text{out,p}}$ , the median value for  $R_{\text{out,t}}$  would be  $1.15 R_p$ , and the median value for the true crossing time would be  $0.58 R_p / v_{\text{out,p}}$ . The net effects of this are that the true  $\text{KE}_t$  is 4 times  $\text{KE}_p$ ,  $p_t = 2p_p$ , and the true outflow rates for  $\dot{M}$ ,  $\dot{p}$ , and  $\text{KE}$  will be larger than the projected values by factors of 1.7, 3.5, and 6.9, respectively.

## 5. Discussion

Our analyses of the NIRSpc data cube confirm the presence of spatially extended fast outflows in TNJ1338. The new data

reveal prominent, highly complex, filamentary structures that extend from the host galaxy northward for a projected angular distance of  $\sim 1''66$  or  $\sim 12 \text{ kpc}$ . We detect high-velocity gas clouds ( $|v| > 800 \text{ km s}^{-1}$ ) marked by broad lines ( $W_{50} \sim 1000 \text{ km s}^{-1}$ ) and extended emission tracing a bubble-like morphology. This is aligned with the radio lobe and indicates jet-driven feedback. Interestingly, we detect some high-velocity gas centered in the host galaxy as well (Figure 4 right panel), which is spatially compact and tend to be quite concentrated within the inner few kiloparsecs. This is possibly driven by radiative feedback from the central obscured quasar in TNJ1338. The mechanical feedback driven by the radio jet, however, affects the gas kinematics to larger distances and over a much larger volume. In this section, we revisit the emission-line luminosity, outflow kinematics, and energetics to discuss



**Table 1**  
Measured Global Properties of TNJ1338

$z$	$M_*$ $M_\odot$	$L_{[\text{O III}]}$ $\text{erg s}^{-1}$	$L_{\text{jet}}$ $\text{erg s}^{-1}$	$L_{\text{AGN}}$ $\text{erg s}^{-1}$	$M_{\text{gas}}$ $M_\odot$	$\dot{M}_{\text{out}}$ $M_\odot \text{ yr}^{-1}$	$\text{KE}_{\text{gas}}$ $\text{erg}$	$\dot{\text{KE}}_{\text{outflow}}$ $\text{erg s}^{-1}$	$\dot{p}_{\text{outflow}}$ $\text{dyne}$	LAS kpc
4.104	$10^{10.9}$	$5.6 \times 10^{45}$	$1.4 \times 10^{47}$	$2.15 \times 10^{48}$	$4.8 \times 10^9$	497	$2.7 \times 10^{58}$	$1.01 \times 10^{44}$	$2.06 \times 10^{36}$	36

**Notes.** All quantities reported here are integrated over the whole galaxy. The columns are redshift, stellar mass, extinction-corrected [O III] 5007 Å luminosity, radio-jet mechanical energy derived from 1.4 GHz radio luminosity, AGN bolometric luminosity derived from the dust-corrected [O III], ionized gas mass, mass outflow rate, kinetic energy of the outflow, kinetic power of the outflow, momentum rate, and the radio linear size (LAS), respectively. The ionized gas mass, outflow rate, kinetic energy of the emission-line gas, and momentum rate are all derived per spaxel primarily using the [O III] 5007 Å emission in a spatially resolved manner, as shown in Figure 10. The values reported in this table are obtained by spatially integrating these resolved estimates over the spaxels where the [O III] S/N > 3 (per spaxel). Note, the  $\dot{M}_{\text{out}}$ ,  $\text{KE}_{\text{gas}}$ , and  $\dot{\text{KE}}_{\text{outflow}}$  values reported here do not include corrections for projection effects (see Section 4.3) and hence are lower limits.

the source of the ionized gas and the driving mechanisms of the jet-driven outflow.

### 5.1. Photoionization from the Central Quasar?

The first natural question is what ionizes the massive amount of  $\sim 5 \times 10^9 M_\odot$  gas extending for tens of kiloparsecs from the nuclear region of the host galaxy. The most plausible explanation is that the [O III]-emitting nebula is part of the interstellar or circumgalactic medium of the host galaxy TNJ1338, which is photoionized by the obscured quasar residing in the host galaxy and get ejected outwards by the large-scale outflow. We will return to the discussion about the nature and the source of the outflow in Section 5.3; here we explore whether the central quasar is the primary source of ionization in this galaxy.

The rest-frame UV continuum from a QSO is typically more than 2 orders of magnitude more luminous than what would be required to explain the typical observed [O III] luminosities of the nebulae (Elvis et al. 1994). Hence, photoionization by the quasar is unavoidable. To check if similar photoionization is occurring in TNJ1338, we assume a model in which the nebulae are in photoionization equilibrium with the diffuse QSO radiation field (similar to Crawford et al. 1988; Baum & Heckman 1989; Heckman et al. 1991). The electron number density of a photoionized cloud ( $n_e$ ) located a distance  $r$  from an ionizing source with a photon luminosity ( $Q$ ) and characterized by an ionization parameter  $U$  (defined as the ratio of ionizing photons to electrons in the cloud) is given by:

$$n_e = \frac{Q}{4\pi r^2 U c}. \quad (4)$$

Our measured values of  $n_e$  range between 400–1200  $\text{cm}^{-3}$ , with a median value of 570  $\text{cm}^{-3}$ . Value for  $U$  is inferred from the comparison of the relative strengths of high-ionization and low-ionization lines to photoionization models. We use the dust-corrected [O III]  $\lambda 5007$ /[O II]  $\lambda \lambda 3726, 3729$  line ratio with assumed solar metallicity to determine a median ionization parameter  $U \sim 10^{-2}$ . Assuming  $r \approx 10$  kpc yields  $Q = 1.9 \times 10^{57} \text{ s}^{-1}$ . Assuming a mean spectral energy distribution of a quasar (Elvis et al. 1994), the relation between AGN bolometric luminosity ( $L_{\text{AGN}}$ ) and the ionizing luminosity ( $Q$ ) is  $L_{\text{AGN}}/Q = 9.5 \times 10^{-11} \text{ erg}$ , which translates to  $L_{\text{AGN}} = 1.8 \times 10^{47} \text{ erg s}^{-1}$ . This is about an order of magnitude smaller than the  $L_{\text{AGN}} = 2.15 \times 10^{48} \text{ erg s}^{-1}$  derived from the far-infrared and [O III]  $\lambda 5007$  luminosities (see Table 1). Thus, the central quasar seems more than capable of being the primary ionizing source, provided that a sufficient fraction of the ionizing radiation can escape the nucleus. The strong alignment of the extended emission-line gas and the radio source (Figure 11) implies that

this gas is photoionized by the radiation that escapes the central quasar in a radiation cone that is aligned along the jet axis.

We should note however that we cannot entirely exclude ionization by shocks driven by the radio jet or its cocoon. The plausible scenario that emerges from the observations is that the jets plow through the surface, interact with the surrounding medium, and create shocked ISM gas driven out at high velocity. In fact, it has been observed before that radio sources with shock-dominated ionization states are expected to show the highest FWHM of [O II]  $\lambda 3727$  emission (Best et al. 2000). The high FWHM values ( $> 1000 \text{ km s}^{-1}$ ) observed in our system hint at the contribution of shocks in the ionization states of the gas. The ionization properties and possible role of fast shocks are further explored in Saxena et al. (2024) via standard Baldwin–Phillips–Terlevich diagrams (Baldwin et al. 1981).

### 5.2. Comparison of TNJ1338 with Radio-quiet Type 1 Quasistellar Objects Studied with JWST/NIRSpec Integral Field Unit Data

Our study presents the first detailed, spatially resolved view of a  $z > 4$  radio galaxy hosting outflow. Here, we compare the outflow properties of TNJ1338 with four other high-redshift ( $z > 1.5$ ) Type 1 unobscured quasar host galaxies recently studied with JWST/NIRSpec IFU data, as reported in Cresci et al. (2023), Marshall et al. (2023), and Veilleux et al. (2023).

The outflow velocity and [O III] line widths for TNJ1338, characterized by moment 1 and  $W_{50}$  values, exceed 1200–1500  $\text{km s}^{-1}$ . Figure 12 shows the distribution of  $W_{80}$  measurements for our radio galaxy TNJ1338 (in black), compared with five other Type 1 quasars (in yellow, magenta, salmon, blue, and green) with published JWST NIRSpec IFU data. For published sources who do not report  $W_{80}$  measurements, we assume  $W_{80}$  is approximately equal to twice the moment 2 values. We see that the kinematics for our system is the most extreme, with  $W_{80}$  reaching 2500–3000  $\text{km s}^{-1}$  for some locations in the galaxy, with typical values ranging between 800–2900  $\text{km s}^{-1}$ . Although high  $W_{80}$  measurements are not unexpected for luminous AGN, as shown in various studies (Bischetti et al. 2017; Perna et al. 2017; Coatman et al. 2019; Temple et al. 2019; Villar Martín et al. 2021), the high velocities over an extended region as observed in TNJ1338 are indicative of extreme outflowing nebulae.

For TNJ1338, the total mass outflow rate ( $\dot{M}_{\text{out}} \sim 500 M_\odot \text{ yr}^{-1}$ ) is roughly similar to the SFR estimated from the host galaxy region by Duncan et al. 2023, which is  $\sim 490 M_\odot \text{ yr}^{-1}$ . This SFR estimate is in agreement with the estimate of  $\sim 461 M_\odot \text{ yr}^{-1}$  derived from the infrared continuum (Falkendal et al. 2019). Note both these SFR estimates are possibly upper limits due to significant contamination from AGN photoionization.

**Table 2**

Measured Properties at the Host (H) and Nebular (N) Region of TNJ1338, Averaged/Integrated over the Spatial Apertures Marked as ‘‘H’’ and ‘‘N’’ in Figure 1

Location	$L_{[\text{O III}]}$ erg s $^{-1}$	$L_{\text{H}\alpha}$ erg s $^{-1}$	$n_e$ cm $^{-3}$	$\bar{W}_{50}$ km s $^{-1}$	$\bar{W}_{80}$ km s $^{-1}$	$\Delta_{\text{peak}}$ km s $^{-1}$	$M_{\text{gas}}$ $M_{\odot}$	$\dot{M}_{\text{out}}$ $M_{\odot}$ yr $^{-1}$	$\text{KE}_{\text{gas}}$ erg	$\text{KE}_{\text{outflow}}$ erg s $^{-1}$
Host	$2.39 \times 10^{45}$	$7.37 \times 10^{44}$	570	489	1064	125	$2.8 \times 10^9$	234	$6 \times 10^{57}$	$2.05 \times 10^{43}$
Nebula	$3.18 \times 10^{45}$	$7.73 \times 10^{44}$	610	778	1668	748	$1.9 \times 10^9$	264	$2 \times 10^{58}$	$8 \times 10^{43}$

**Notes.** The columns are: location in the galaxy (whether host or nebular), extinction-corrected [O III] 5007 Å luminosity integrated over the host/nebular region, extinction-corrected H $\alpha$  luminosity, mean electron density, mean [O III]  $W_{50}$  (line width containing 50% of the emission-line flux), mean  $W_{80}$  (line width containing 80% of the emission-line flux), the peak-to-peak separation between the two fitted kinematic components of the [O III] line profile calculated per spaxel (Figure 7) and averaged over the host/nebular apertures, ionized gas mass, mass outflow rate, kinetic energy, and kinetic power of outflows. The gas mass, outflow rate, and outflow energy are all computed per spaxel and integrated over spatial apertures bounding the host and nebular region. Note, the  $\dot{M}_{\text{out}}$ ,  $\text{KE}_{\text{gas}}$ , and  $\text{KE}_{\text{outflow}}$  values reported here do not include corrections for projection effects (see Section 4.3) and hence are lower limits.

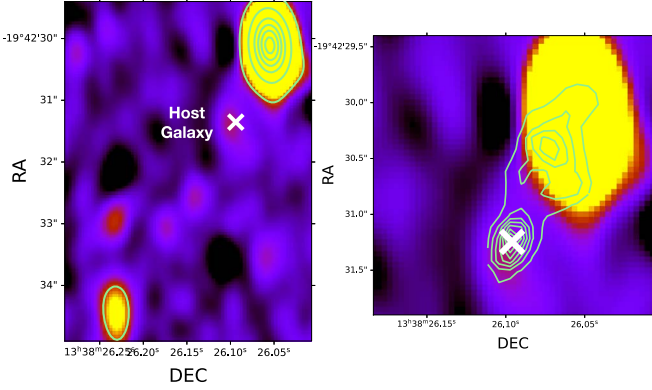
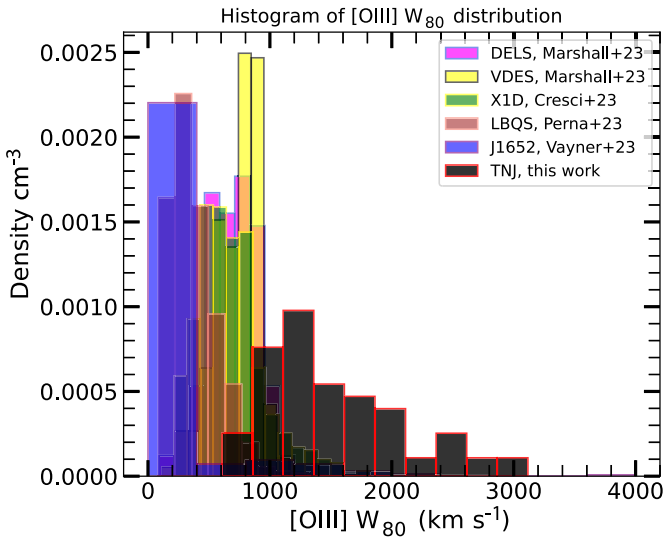


**Figure 11.** Left panel: VLA 4.5 GHz radio continuum image for the double-lobed radio source TNJ1338 with green contours showing 1%, 10%, 30%, 50%, 70%, and 90% of the peak radio intensity. Right panel: zoomed-in radio image around the bright northern radio lobe with [O III]  $\lambda 5007$  emission flux from NIRSpec overlaid on top in green contours. The continuum from the host galaxy location is marked with a white cross on both panels. The bright radio lobe is spatially aligned with the [O III]-enhanced nebular region. There is an astrometric inaccuracy of the order of  $\sim 0''.02$  between the VLA and JWST/NIRSpec maps.

large distances. Unlike our system, the Type 1 QSO X1D2028 observed recently with JWST/NIRSpec as part of the JWST ERS-1335 program, shows a much lower mass loading factor  $\eta \sim 0.04$  (Veilleux et al. 2023) and very low mass outflow rate ( $\sim 6 M_{\odot}$  yr $^{-1}$ ; Cresci et al. 2023) in spite of hosting a powerful quasar. It is worth noting that this same quasar was previously reported to host a much higher mass outflow rate ( $\sim 100 M_{\odot}$  yr $^{-1}$ ) using ground-based spectral analyses and with a generic assumption of the electron density. With the improved JWST spectra, upgraded velocity values from better-resolved kinematics studies, and better estimates of density from [S II]  $\lambda\lambda 6717, 6731$  lines, the mass outflow rate turned out to be  $\sim 15$  times lower.

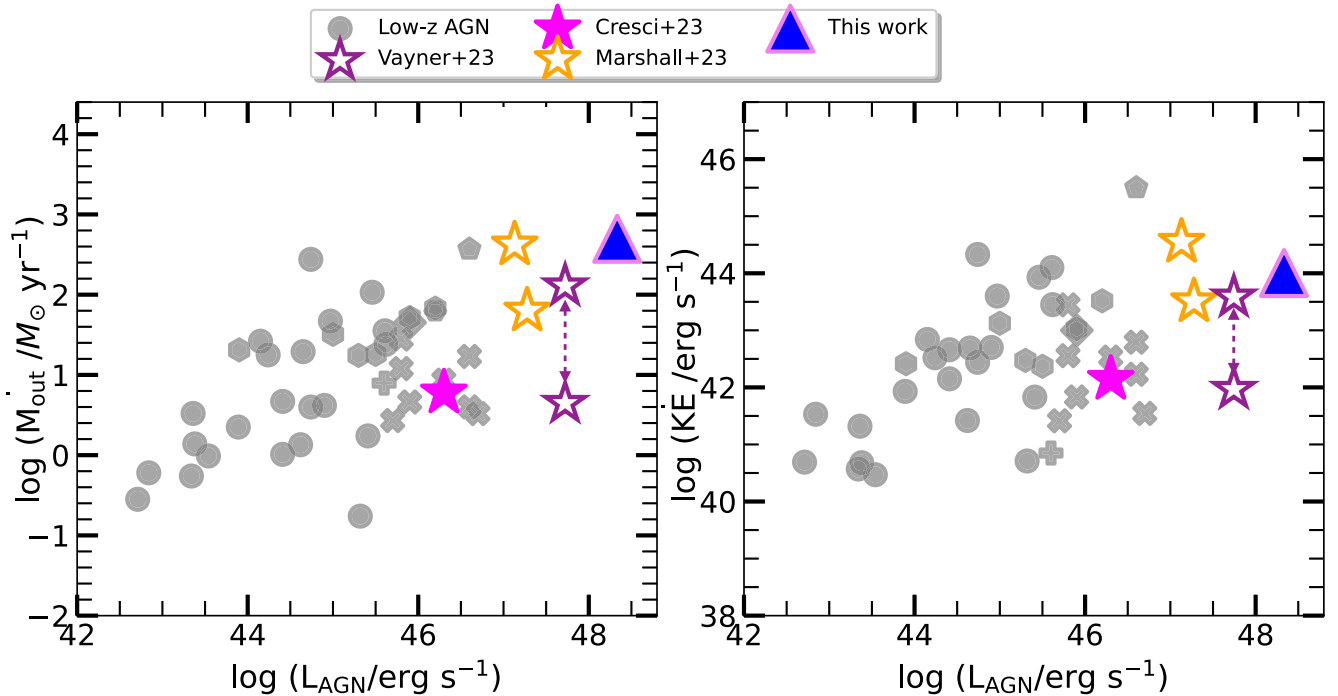
The two Type 1 QSOs from Marshall et al. (2023) have reported mass loading factors greater than unity (1.6 and 2). However, these mass outflow estimates are possibly highly uncertain, given that electron densities were not directly measured from [S II]  $\lambda\lambda 6717, 6731$  line ratios owing to their nondetection, and were assumed to be a generic value. This can significantly affect the mass outflow rate estimates (63 and 420  $M_{\odot}$  yr $^{-1}$ ). Veyner et al. (2024) studied a powerful quasar-driven outflow at  $z = 3$  and measured a mass outflow rate that declined steeply with radius, falling from  $\dot{M}_{\text{out}} = 100 M_{\odot}$  yr $^{-1}$  at a radius of 1 kpc to  $\sim 3 M_{\odot}$  yr $^{-1}$  at 5 kpc. In most of these cases, the outflow velocities are also tentative, since they assume the highest outflow velocity in the energetics calculation, which might not be representative of the major part of the outflowing region.

Figure 13 (left panel) shows the mass outflow rates ( $\dot{M}_{\text{out}}$ ) versus bolometric AGN luminosity ( $L_{\text{AGN}}$ ) for TNJ1338 (triangle) compared with published JWST Type 1 QSOs at high  $z$  with spatially resolved outflows (shown as stars; Cresci et al. 2023; Marshall et al. 2023) and a compilation of low-redshift AGN with similar outflow signatures from the literature (gray symbols; Nesvadba et al. 2006; Brusa et al. 2016; Revalski et al. 2018; Shimizu et al. 2019; Dall’Agnol de Oliveira et al. 2021; Revalski et al. 2021; Kakkad et al. 2022). We choose only those low- $z$  studies that use a directly measured electron density and outflow velocity in the calculation. Of the four high- $z$  Type 1 QSOs shown, only one has a density measurement and that is shown with a filled star symbol. The rest are shown with unfilled star symbols. We show the Veyner et al. (2024) outflow rate measurements as two separate points (purple stars) connected by a dashed arrowhead line. These represent the outflow rates reported at 1 kpc and 5 kpc radial distances, respectively, as reported from their radial profiles. However, we do not sum up those estimates to derive a single measurement, as summing the



**Figure 12.** Histogram of the distribution of  $W_{80}$  values in radio-quiet quasars observed with JWST/NIRSpec previously, compared to our radio-loud galaxy TNJ1338 (black). TNJ1338 shows the highest line widths and the most extreme kinematics in the emission-line gas.

The lower limit on the mass loading factor  $\eta = \dot{M}/\text{SFR}$  is thus  $\sim 1.01$ . The high mass outflow rate and mass loading imply that the outflow can efficiently displace a significant amount of gas to



**Figure 13.** Left panel: globally integrated mass outflow rate vs. AGN bolometric luminosity reported in the literature using a variety of IFU/long-slit spectroscopy. Gray symbols indicate low-redshift quasars (Nesvadba et al. 2006; Brusa et al. 2016; Revalski et al. 2018; Dall’Agnol de Oliveira et al. 2021; Revalski et al. 2021; Kakkad et al. 2022), the colored stars indicate JWST/IFU observations of radio-quiet quasars at high redshifts (Cresci et al. 2023; Marshall et al. 2023; Veilleux et al. 2023), and the unfilled stars represent measurements where the electron density estimates are assumed and not directly measured due to nondetection of the [S II]  $\lambda\lambda 6717, 6732$  lines. Our radio galaxy source TNJ1338, shown with a blue triangle, occupies the highest end of the distribution, with the highest outflow rates and the strongest AGN bolometric luminosity observed; but is overall consistent if we extrapolate the trend visible in radio-quiet quasars at high  $z$ . Right panel: kinetic outflow power vs. AGN bolometric luminosity for literature compiled objects (gray symbols and colored stars) compared to TNJ1338 (triangle). The kinetic outflow power and the bolometric AGN luminosity recorded for TNJ1338 are some of the strongest ever measured at similar redshifts in radio-quiet quasars.

contribution from different radii leads to an erroneous global outflow rate due to the specific way they calculate outflow rates. Our object lies at the highest end of both  $\dot{M}_{\text{out}}$  and  $L_{\text{AGN}}$  values, but is overall consistent with the linear correlation observed between these two quantities at low redshift. A similar observation can be made in the kinetic power of the outflowing gas versus AGN luminosity diagram, shown in the right panel.

The total kinetic power of the outflowing emission-line gas in TNJ1338 is  $1.0 \times 10^{44}$  erg s $^{-1}$ . Various feedback models and simulations predict that for feedback to launch a blastwave sufficiently powerful to entrain gas and to inject adequate energy into the ISM, the kinetic power of the outflow needs to be about 5%–7% of the AGN bolometric luminosity. On the other hand, a “two-stage” model was proposed by Hopkins & Elvis (2010) that stated that initial feedback from the central quasar needs to only initiate a moderate wind in the low-density hot gas, which reduces the required energy budget for feedback by an order of magnitude. In this model, outflow kinetic power needs to be a minimum of  $\sim 0.5\%$  of the AGN bolometric luminosity. TNJ1338 has a kinetic power  $\text{KE}_{\text{outflow}} \sim 0.1\%$  of  $L_{\text{AGN}}$ , indicating that the outflow itself may not be able to deposit an enormous amount of energy which is capable of altering the surrounding ISM conditions. However, we should note two things. First, this kinetic power is only a lower limit, since it does not include corrections for projection effects (Section 4.3). Second, the NIRSspec data only probe the warm ionized gas phase of the outflow; the other phases of the outflow—like the hot phase or the cold molecular phase—

may carry more energetic outflows and the total kinetic power (summing all phases) may well exceed the 0.5% threshold predicted by the two-stage feedback model.

### 5.3. Radio-jet Powered Feedback

The VLA images of TNJ1338 (Figure 1) show two blobs located to the north and south in opposite directions from the nuclear region, indicating a bipolar radio jet (Pentericci et al. 2000). We have presented multiple pieces of evidence that the energy deposited by these powerful radio jets is responsible for the extraordinary kinematics exhibited by the ionized gas (traced by [O III]  $\lambda 5007$ ) over the region extending from roughly 3 kpc to 10 kpc to the north of the nucleus (although there can always be a nonzero contribution from accretion disk driven winds, similar to Silpa et al. 2021). If this bright and kinematically disturbed nebular (N) region represents the site of a collision of a jet with a massive gas cloud, it would naturally explain why the northern radio lobe is about 4 times brighter than the southern lobe, and about 3 times closer to the nucleus. This is also in agreement with numerical simulations of jets modeled in a clumpy ISM (Dutta et al. 2023), which have shown that the radio jet undergoes deceleration when the jet head is obstructed by dense clouds, and results in a strong shock that creates radio hot spots. We also showed that the kinematics in this region are far more extreme than what has been observed in JWST NIRSspec IFU data for outflows in radio-quiet QSOs with bolometric luminosities similar to TNJ1338 (Figure 12).

In this section, we will quantify the nature of the jet–ISM interaction that we are witnessing. We begin with a comparison



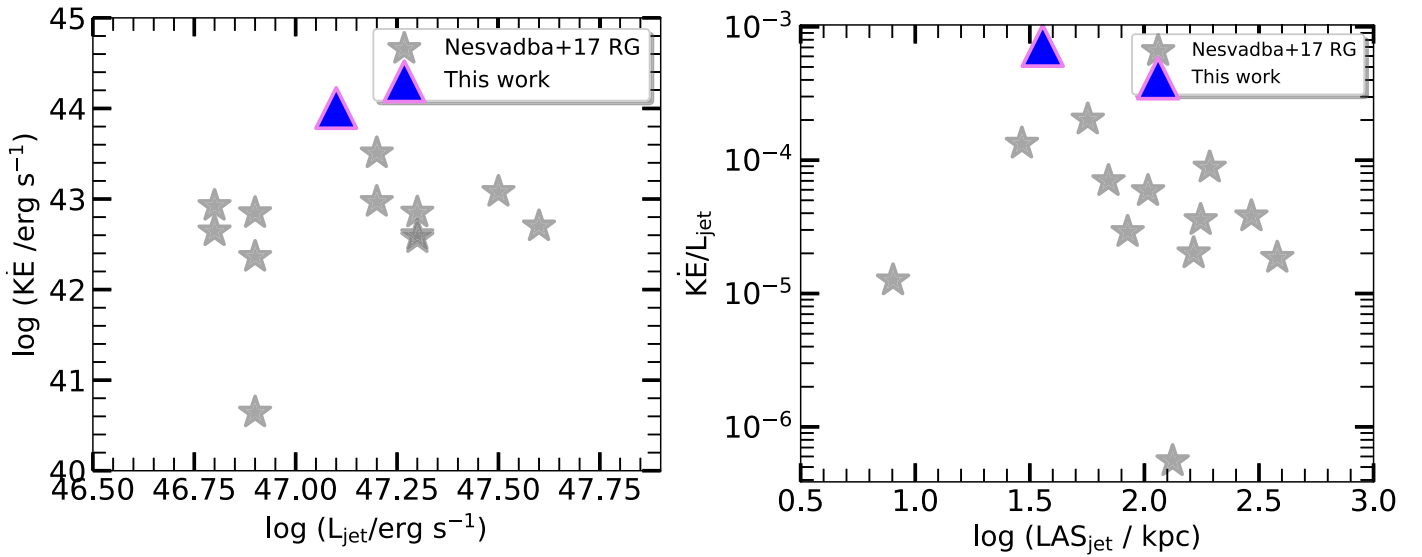


**Figure 14.** Left panel: kinetic power of the outflows vs. the radio-jet mechanical energy for high- $z$  (median  $z \sim 2.5$ ) radio galaxy sample reported in N17 (gray stars), and TNJ1338 from this work (blue triangle). Right panel: ratio of the outflow kinetic power and jet mechanical energy plotted against radio size (in kiloparsecs) for the same objects. TNJ1338 has the highest kinetic power of outflows, with  $\text{KE}_{\text{outflow}}$  about an order of magnitude larger than the median value for the other radio galaxies in the N17 sample. No corrections for projection effects (see Section 4.3) have been made. The radio size of TNJ1338 is also relatively small, suggesting that the transfer of kinetic energy from the jet to the gas is facilitated by the higher gas densities expected at smaller radii.

of the energetics of the outflow in TNJ1338 to those of the other HZRGs investigated by Nesvadba et al. (2017, N17 hereafter) using ground-based NIR IFU data. TNJ1338 has a similar radio luminosity (and inferred jet kinetic energy flux) with most of the N17 sample but differs in terms of its redshift ( $z = 4.104$  versus the N17 median of  $z = 2.5$ ) and the compact size of the radio source ( $\sim 36$  kpc versus the N17 median of  $\sim 100$  kpc). In fact, TNJ1338 is in the N17 sample, but its optical emission-line region was spatially unresolved from ground-based observations. With the JWST/NIRSpec revealing extended ionized gas component in TNJ1338, we aim to make an “apples-to-apples” comparison of the energetics of this emission-line gas with the rest of the HZRGs from the N17 sample. N17 computed two estimates of  $\text{KE}_{\text{outflow}}$ , but these used entirely different approaches than ours. Hence, we do not use those for comparison. We have used the data tabulated in N17 to measure  $\text{KE}_{\text{outflow}}$  ourselves for the other HZRGs in exactly the same way as we calculated for TNJ1338, as described in Section 4.3. The results are shown in Figure 14. In the left panel, we plot  $\text{KE}_{\text{outflow}}$  versus  $L_{\text{jet}}$  for TNJ1338 (blue triangle) and the N17 radio galaxy sample (gray stars). There is no evident correlation, but this may be due in part to the small range spanned in  $L_{\text{jet}}$  (a factor of  $\sim 6$ ). TNJ1338 is an outlier, with  $\text{KE}_{\text{outflow}}$  about an order of magnitude larger than the median value for the other radio galaxies.

To investigate this further, in the right panel, we plot the ratio of  $\text{KE}_{\text{outflow}}/L_{\text{jet}}$  versus the size of the radio source. There is a trend for the former ratio to increase as the radio source size decreases, with TNJ1338 lying at one end of the distribution. This suggests that the transfer of kinetic energy from the jet to the gas is facilitated by the higher gas densities expected at smaller radii. However, it is important to note that in the case of TNJ1338, the kinetic energy flux in the gas is less than 0.1% of the jet kinetic energy flux. Even correcting for projection effects (Section 4.3) the kinetic energy flux will be less than 1% of the jet kinetic energy flux.

We adopted our method of computing outflow rates in Section 4.3 to be as similar as possible to those in previous JWST NIRSpec IFU investigations of outflows of ionized gas in high- $z$  radio-quiet QSOs, so that TNJ1338 could be placed into this context (see Figure 14). This method implicitly assumes that the observed gas has traveled from the nucleus to its current location at its currently observed velocity (that is, the mass and kinetic energy of the gas are converted into fluxes using a crossing time of  $t_{\text{cross}} = R/v_{\text{out}}$ ). While this is a natural choice, it may be inappropriate for the situation seen in TNJ1338 (or other jet-driven outflows). In this case, the appropriate timescale for the outflow would be the lifetime of the radio source ( $t_{\text{RS}}$ ). This can be significantly shorter than  $t_{\text{cross}}$ . In this case, the observed gas has only been moving at  $v_{\text{out}}$  for a timescale  $t_{\text{RS}}$ , meaning it has moved only a relatively small distance from its initial location. We can quantify this picture in the case of TNJ1338. To estimate the radio source lifetime  $t_{\text{RS}}$ , we need to take the distance of the northern radio lobe from the nucleus (8.8 kpc) and divide it by an estimate of the outward velocity of the radio lobe ( $v_{\text{RL}}$ ). We will do this in two ways: one empirical and one based on simple analytic theory. We begin with the latter since it provides a simple conceptual framework for interpreting the data.

Begelman & Cioffi (1989) presented a simple theoretical model for how a radio jet would interact with ambient gas. In this model, the jet encounters dense gas and terminates in a strong shock, producing intense radio emission from a “hot spot.” The immensely overpressured shocked jet fluid then expands laterally and back flows to create an expanding ellipsoidal “cocoon” that pushes the gas and drives outflows into the surrounding gas. This can result in the observations of high-velocity gas coincident with the jet axis and radio hot spots. This also agrees with high-resolution hydrodynamic jet simulations which have found similar wide cocoons expanding through the low-density diffuse phase (Dutta et al. 2023). Figure 15 summarizes this picture. In this scenario, they

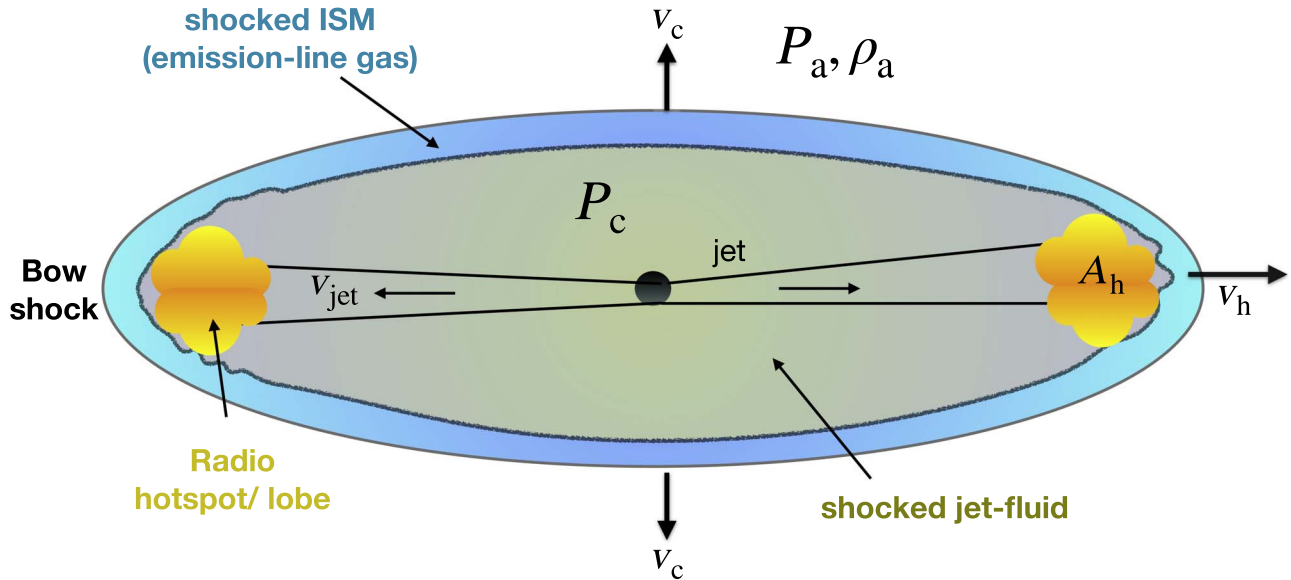


**Figure 15.** Schematic diagram to summarize the proposed scenario in TNJ1338, inspired by the model proposed by Begelman & Cioffi (1989). The radio jet, traveling with a speed of  $v_{\text{jet}}$ , terminates with the formation of radio lobes/hot spots, with a cross-sectional area  $A_h$ . While the jets plow through the surface, they are enveloped in a cocoon consisting of shocked jet-fluid material, which is wrapped in a layer of shocked ISM ambient gas. This thin layer of shocked ISM emission-line gas is possibly visible in the JWST/NIRSpec IFU data as extended [O III] emission, spatially aligned with the radio lobes.  $P_c$  and  $P_a$  indicate the pressure inside and outside the cocoon respectively. If the cocoon is overpressured, i.e.,  $P_c > P_a$ , it drives a shock laterally—thus expanding the cocoon sideways with a velocity  $v_c$ , and with a velocity  $v_h$  in the orthogonal direction. Utilizing the dynamical timescale  $\sim 3$  Myr derived from this simplistic picture, we compute the total kinetic energy supplied by the radio jet and find that the kinetic energy is transferred very inefficiently from the jets to the emission-line gas ( $\text{KE}_{\text{gas}}/\text{KE}_{\text{jet}} \sim 10^{-3}$ ), consistent with the right panel of Figure 14.

showed that the velocity at which the hot spot advances is given by:

$$v_h = \left( \frac{L_{\text{jet}}}{(A_h v_{\text{jet}} \rho_a)} \right)^{1/2}. \quad (5)$$

Here,  $L_{\text{jet}}$  is the rate at which the radio jet transports kinetic energy,  $A_h$  is the cross-sectional area of the hot spot,  $v_{\text{jet}}$  is the jet velocity (which is taken as  $c$  in Begelman & Cioffi 1989), and  $\rho_a$  is the mean ambient gas density. These are marked in Figure 15. For TNJ1338 the estimated value for  $L_{\text{jet}}$  is  $7 \times 10^{46}$  erg  $\text{s}^{-1}$  for the northern jet alone (Nesvadba et al. 2017). Based on the lateral extent of the northern radio lobe over which the radio flux drops by 50% in Figure 1 & 11, we estimate  $A_h = 3 \times 10^{43}$   $\text{cm}^2$ . We take  $\rho_a = 1.6 \times 10^{-24}$   $\text{cm}^{-3}$  such that the total gas mass is  $10^{11} M_{\odot}$  interior to a radius of 10 kpc (similar to the galaxy stellar mass, Table 1). With these values, the predicted value is  $v_h \sim 2200$   $\text{km s}^{-1}$ , corresponding to a radio source lifetime  $t_{\text{RS}} \sim 3.9$  Myr.

Using this conceptual framework, we can get an independent empirical estimate of the radio source lifetime using the results on the double-peaked emission-line profiles lying along the jet axis (Figure 7). In the Begelman & Cioffi (1989) model these line profiles trace the lateral expansion velocity of the cocoon (with one line each from the front and back sides). The mean peak separation, i.e.,  $v_c \sim 900$   $\text{km s}^{-1}$ , and the lateral extent of the region is about 3 kpc. Dividing this size by this velocity implies a dynamical age of about 3.3 Myr, which is close to the theoretical estimate above. In comparison,  $t_{\text{cross}}$  for the emission-line region (see above) is about 10 Myr. In this picture in which the gas is very rapidly accelerated for only a short time, it makes more sense to compare the total kinetic energy in the gas to the total kinetic energy transported by the jets (rather than comparing the KE). For a radio source lifetime

of 3.3 Myr and a two-sided jet kinetic energy flux  $L_{\text{jet}}$  of  $1.4 \times 10^{47}$  erg  $\text{s}^{-1}$ , the total amount of injected energy is  $E_{\text{jet}} \sim 1.4 \times 10^{61}$  erg. This can be compared to the total kinetic energy measured in the outflowing ionized gas  $\text{KE}_{\text{outflow}} \sim 3 \times 10^{58}$  erg (or  $1.2 \times 10^{59}$  erg for a median correction for projection effects, see Section 4.3). This implies that kinetic energy is transferred very inefficiently from the jets to the emission-line gas (consistent with the results in Figure 14 above).

Next, we use Equation (6) in Begelman & Cioffi (1989), to estimate the pressure in the northern cocoon, using the values above for  $L_{\text{jet}}$  and  $A_h$ , a cocoon length of 8.8 kpc, and a cocoon half width of 1.5 kpc. This yields  $P_c = 3.4 \times 10^{-7}$  dyne  $\text{cm}^{-2}$ . This is roughly  $10^2$  times larger than the pressure measured using the [S II]-derived densities and an assumed temperature for photoionized gas of  $\sim 10^4$  K (Osterbrock & Ferland 2006). This implies that the gas we see does not lie inside the cocoon, but instead represents ambient lower-pressure gas surrounding (and being accelerated by) the cocoon.

The result that the emission-line gas carries only a small fraction of the jet kinetic energy should not be surprising. If the cocoon is traveling outward at  $v_h \sim 2200$   $\text{km s}^{-1}$  and expanding laterally at  $v_c \sim 500$   $\text{km s}^{-1}$  (see above), the shocks that these motions drive into the ambient gas correspond to postshock temperatures of  $\sim 80$  MK and 4 MK, respectively. Thus, the bulk of the deposited energy would be in the form of hot X-ray-emitting gas. In fact, as noted in the Introduction, TNJ1338 has been detected in X-rays (Smail & Blundell 2013). The X-ray emission is aligned with the radio axis and is extended by about 30 kpc, but no detailed spatial coincidence exists between the X-ray and radio emission. We suggest that the X-ray emission may arise in shocks driven by the expanding cocoon. The X-ray luminosity is  $3 \times 10^{44}$  erg  $\text{s}^{-1}$ , which, while substantial, is far less than the kinetic energy flux carried by the jets. This would imply that the radiative cooling

time of the hot gas is much longer than the radio source's lifetime.

## 6. Conclusions

In this paper, we present the JWST NIRSpec/IFU observations (JWST GO 1964: coPIs: Overzier and Saxena) of TNJ1338, a radio galaxy at  $z = 4.104$ , hosting an obscured quasar at the nucleus. This source is a double-lobed radio galaxy as revealed from existing VLA radio observations, with the northern lobe  $\sim 4$  times brighter than the southern lobe, and about 3 times closer to the nucleus. This bright radio lobe spatially overlaps with an extended ionized gas nebula which shows some of the fastest-moving outflows compared to other unobscured quasar populations recently studied with JWST. We map the location of these fast-moving outflows, characterize the spatially resolved outflow kinematics and energetics at kiloparsec-scale resolution using rest-frame optical emission lines using JWST/NIRSpec IFU, and construct a simplistic model to explain the radio-jet-driven feedback possibly at play. The following are the main conclusions:














1. We detect ionized outflow with velocities exceeding  $900 \text{ km s}^{-1}$  and broad line profiles with line widths exceeding  $1200 \text{ km s}^{-1}$  (mean  $W_{50} \sim 800 \text{ km s}^{-1}$ , mean  $W_{80} \sim 1600 \text{ km s}^{-1}$ ) about  $\sim 5 \text{ kpc}$  away from the central nucleus of the galaxy. The outflowing gas extends up to  $\sim 15 \text{ kpc}$  in projection from the center, roughly cospatial with the bright northern radio lobe.
2. A massive amount of ionized gas of mass  $\sim 5 \times 10^9 M_{\odot}$  is detected, with a total integrated mass outflow rate of  $497 M_{\odot} \text{ yr}^{-1}$ . The mass loading factor of unity indicates that a significant part of the ionized gas is displaced from the host galaxy via outflows. The total kinetic power deposited by the outflows is  $\sim 1 \times 10^{44} \text{ erg s}^{-1}$ . We present carefully measured estimates of spatially resolved mass outflow rates and kinetic energy of the line-emitting gas for the first time for a  $z > 4$  AGN host galaxy.
3. The extended ionized gas nebula detected likely formed due to photoionization by the obscured quasar residing in the host galaxy with some contribution from shocks. However, the powerful radio jets are responsible for the large-scale outflows and the extraordinary kinematics exhibited by the ionized gas. Our hypothesis is that the radio jet terminates in a strong shock, producing radio hot spot/lobes. The immensely overpressured shocked jet fluid then expands laterally and back flows to create an expanding ellipsoidal cocoon that entrains/accelerates the surrounding gas outwards, creating this high-velocity gas. This scenario explains the kinematics and the spatial alignment between the northern radio lobe and the optical emission-line gas seen in TNJ1338.
4. The total kinetic energy injected by the radio jet is  $\sim 1 \times 10^{61} \text{ erg}$ , which is roughly 3 orders of magnitude larger than the total kinetic energy measured in the outflowing ionized gas. This implies that kinetic energy is transferred very inefficiently from the jets to the emission-line gas. This is unsurprising, since the expanding cocoons drive shocks corresponding to postshock temperatures of a few million kelvin. Hence the bulk of the deposited energy would be in the form of hot X-ray-emitting gas.
5. TNJ1338 has a kinetic efficiency ( $\dot{K}E_{\text{outflow}}/L_{\text{AGN}} \sim 0.1\%$ ), indicating that the outflow itself may not be able to deposit an enormous amount of energy which is capable of altering the surrounding ISM conditions.

## Acknowledgments

N.R. and T.H. thank Anton Koekemoer for their help in the registration of the NIRSpec cube with the NIRCAM mosaics. K.J.D. acknowledges support from the STFC through an Ernest Rutherford Fellowship (grant number ST/W003120/1). S.E.I. B. is supported by the Deutsche Forschungsgemeinschaft (DFG) through Emmy Noether grant number BO 5771/1-1. K. É.G. acknowledges the funding received from the HUN-REN Hungarian Research Network and from the Hungarian National Research, Development and Innovation Office (NKFIH), grant number OTKA K134213, and also from the NKFIH excellence grant TKP2021-NKTA-64.

*Software:* Astropy (Astropy Collaboration et al. 2013, 2018, 2022), Scipy (Virtanen et al. 2020), JWST STScI pipeline (Bushouse et al. 2023), and dynesty (Speagle 2020).

## ORCID iDs

Namrata Roy  <https://orcid.org/0000-0002-4430-8846>  
 Timothy Heckman  <https://orcid.org/0000-0001-6670-6370>  
 Roderik Overzier  <https://orcid.org/0000-0002-8214-7617>  
 Aayush Saxena  <https://orcid.org/0000-0001-5333-9970>  
 Kenneth Duncan  <https://orcid.org/0000-0001-6889-8388>  
 George Miley  <https://orcid.org/0000-0003-2884-7214>  
 Krisztina Éva Gabányi  <https://orcid.org/0000-0003-1020-1597>  
 Catarina Aydar  <https://orcid.org/0000-0001-5609-2774>  
 Sarah E. I. Bosman  <https://orcid.org/0000-0001-8582-7012>  
 Huub Rottgering  <https://orcid.org/0000-0001-8887-2257>  
 Laura Pentericci  <https://orcid.org/0000-0001-8940-6768>  
 Masafusa Onoue  <https://orcid.org/0000-0003-2984-6803>  
 Victoria Reynaldi  <https://orcid.org/0000-0002-6472-6711>

## References

- Astropy Collaboration, Price-Whelan, A. M., Lim, P. L., et al. 2022, *ApJ*, **935**, 167  
 Astropy Collaboration, Price-Whelan, A. M., Sipőcz, B. M., et al. 2018, *AJ*, **156**, 123  
 Astropy Collaboration, Robitaille, T. P., Tollerud, E. J., et al. 2013, *A&A*, **558**, A33  
 Baldwin, J. A., Phillips, M. M., & Terlevich, R. 1981, *PASP*, **93**, 5  
 Baron, D., & Netzer, H. 2019, *MNRAS*, **486**, 4290  
 Baum, S. A., & Heckman, T. 1989, *ApJ*, **336**, 702  
 Begelman, M. C., & Cioffi, D. F. 1989, *ApJL*, **345**, L21  
 Best, P. N., Röttgering, H. J. A., & Longair, M. S. 2000, *MNRAS*, **311**, 23  
 Bischetti, M., Feruglio, C., D'Odorico, V., et al. 2022, *Natur*, **605**, 244  
 Bischetti, M., Fiore, F., Feruglio, C., et al. 2023, *ApJ*, **952**, 44  
 Bischetti, M., Piconcelli, E., Vietri, G., et al. 2017, *A&A*, **598**, A122  
 Brusa, M., Perna, M., Cresci, G., et al. 2016, *A&A*, **588**, A58  
 Bushouse, H., Eisenhamer, J., Dencheva, N., et al. 2023, JWST Calibration Pipeline, v1.11.2, Zenodo, doi:10.5281/zenodo.8140011  
 Cano-Díaz, M., Maiolino, R., Marconi, A., et al. 2012, *A&A*, **537**, L8  
 Cicone, C., Maiolino, R., Gallerani, S., et al. 2015, *A&A*, **574**, A14  
 Ciotti, L., Ostriker, J. P., & Proga, D. 2010, *ApJ*, **717**, 708  
 Coatman, L., Hewett, P. C., Banerji, M., et al. 2019, *MNRAS*, **486**, 5335  
 Crawford, C. S., Fabian, A. C., & Johnstone, R. M. 1988, *MNRAS*, **235**, 183  
 Crenshaw, D. M., Fischer, T. C., Kraemer, S. B., & Schmitt, H. R. 2015, *ApJ*, **799**, 83  
 Crenshaw, D. M., Kraemer, S. B., Gabel, J. R., et al. 2003, *ApJ*, **594**, 116  
 Cresci, G., Tozzi, G., Perna, M., et al. 2023, *A&A*, **672**, A128  
 Croton, D. J., Springel, V., White, S. D. M., et al. 2006, *MNRAS*, **365**, 11



- Dall’Agnol de Oliveira, B., Storchi-Bergmann, T., Kraemer, S. B., et al. 2021, *MNRAS*, **504**, 3890
- De Breuck, C., van Breugel, W., Minniti, D., et al. 1999, *A&A*, **352**, L51
- Di Matteo, T., Springel, V., & Hernquist, L. 2005, *Natur*, **433**, 604
- Duncan, K. J., Windhorst, R. A., Koekemoer, A. M., et al. 2023, *MNRAS*, **522**, 4548
- Dutta, R., Sharma, P., Sarkar, K. C., & Stone, J. M. 2023, arXiv:2401.00446
- Elvis, M., Wilkes, B. J., McDowell, J. C., et al. 1994, *ApJS*, **95**, 1
- Fabian, A. C. 2012, *ARA&A*, **50**, 455
- Falkendal, T., De Breuck, C., Lehnert, M. D., et al. 2019, *A&A*, **621**, A27
- Fiore, F., Feruglio, C., Shankar, F., et al. 2017, *A&A*, **601**, A143
- Girdhar, A., Harrison, C. M., Mainieri, V., et al. 2022, *MNRAS*, **512**, 1608
- Harrison, C. M., Alexander, D. M., Mullaney, J. R., & Swinbank, A. M. 2014, *MNRAS*, **441**, 3306
- Heckman, T. M., & Best, P. N. 2023, *Galax*, **11**, 21
- Heckman, T. M., Lehnert, M. D., Miley, G. K., & van Breugel, W. 1991, *ApJ*, **381**, 373
- Hopkins, P. F., & Elvis, M. 2010, *MNRAS*, **401**, 7
- Humphrey, A., Villar-Martín, M., Fosbury, R., et al. 2007, *MNRAS*, **375**, 705
- Intema, H. T., Venemans, B. P., Kurk, J. D., et al. 2006, *A&A*, **456**, 433
- Jarvis, M. E., Harrison, C. M., Mainieri, V., et al. 2021, *MNRAS*, **503**, 1780
- Kakkad, D., Mainieri, V., Padovani, P., et al. 2016, *A&A*, **592**, A148
- Kakkad, D., Sani, E., Rojas, A. F., et al. 2022, *MNRAS*, **511**, 2105
- Koposov, S., Speagle, J., Barbary, K., et al. 2022, joshspeagle/dynesty: v2.0.3, Zenodo, doi:10.5281/zenodo.7388523
- Maiolino, R., Gallerani, S., Neri, R., et al. 2012, *MNRAS*, **425**, L66
- Marshall, M. A., Perna, M., Willott, C. J., et al. 2023, *A&A*, **678**, A191
- McCully, C., Crawford, S., Kovacs, G., et al. 2018, astropy/astrocrappy: v1.0.5, Zenodo, doi:10.5281/zenodo.1482019
- McElroy, R., Croom, S. M., Pracy, M., et al. 2015, *MNRAS*, **446**, 2186
- McNamara, B. R., & Nulsen, P. E. J. 2007, *ARA&A*, **45**, 117
- Meenakshi, M., Mukherjee, D., Wagner, A. Y., et al. 2022, *MNRAS*, **516**, 766
- Miley, G. K., Overzier, R. A., Tsvetanov, Z. I., et al. 2004, *Natur*, **427**, 47
- Mingozzi, M., Cresci, G., Venturi, G., et al. 2019, *A&A*, **622**, A146
- Morganti, R., Oosterloo, T., Tadhunter, C., Bernhard, E. P., & Raymond Oonk, J. B. 2021, *A&A*, **656**, A55
- Mukherjee, D., Bicknell, G. V., Sutherland, R., & Wagner, A. 2016, *MNRAS*, **461**, 967
- Mukherjee, D., Bicknell, G. V., Wagner, A. Y., Sutherland, R. S., & Silk, J. 2018, *MNRAS*, **479**, 5544
- Mukherjee, D., Bodo, G., Mignone, A., Rossi, P., & Vaidya, B. 2020, *MNRAS*, **499**, 681
- Nesvadba, N. P. H., De Breuck, C., Lehnert, M. D., Best, P. N., & Collet, C. 2017, *A&A*, **599**, A123
- Nesvadba, N. P. H., Lehnert, M. D., De Breuck, C., Gilbert, A. M., & van Breugel, W. 2008, *A&A*, **491**, 407
- Nesvadba, N. P. H., Lehnert, M. D., Eisenhauer, F., et al. 2006, *ApJ*, **650**, 693
- Oke, J. B., & Gunn, J. E. 1983, *ApJ*, **266**, 713
- Onoue, M., Kashikawa, N., Matsuoka, Y., et al. 2019, *ApJ*, **880**, 77
- Osterbrock, D. E., & Ferland, G. J. 2006, *Astrophysics of gaseous nebulae and active galactic nuclei* (Sausalito, CA: Univ. Science Books)
- Overzier, R. A., Bouwens, R. J., Cross, N. J. G., et al. 2008, *ApJ*, **673**, 143
- Overzier, R. A., Shu, X., Zheng, W., et al. 2009, *ApJ*, **704**, 548
- Pentericci, L., Van Reeve, W., Carilli, C. L., Röttgering, H. J. A., & Miley, G. K. 2000, *A&AS*, **145**, 121
- Perna, M., Arribas, S., Marshall, M., et al. 2023, *A&A*, **679**, A89
- Perna, M., Lanzuisi, G., Brusa, M., Mignoli, M., & Cresci, G. 2017, *A&A*, **603**, A99
- Revalski, M., Crenshaw, D. M., Kraemer, S. B., et al. 2018, *ApJ*, **856**, 46
- Revalski, M., Meena, B., Martinez, F., et al. 2021, *ApJ*, **910**, 139
- Roy, N., Bundy, K., Cheung, E., et al. 2018, *ApJ*, **869**, 117
- Roy, N., Moravec, E., Bundy, K., et al. 2021, *ApJ*, **922**, 230
- Saito, T., Matsuda, Y., Lacey, C. G., et al. 2015, *MNRAS*, **447**, 3069
- Sanders, R. L., Shapley, A. E., Kriek, M., et al. 2016, *ApJ*, **816**, 23
- Saxena, A., Overzier, R. A., Villar-Martín, M., et al. 2024, *MNRAS*, **531**, 4391
- Shimizu, T. T., Davies, R. I., Lutz, D., et al. 2019, *MNRAS*, **490**, 5860
- Silpa, S., Kharb, P., O’Dea, C. P., et al. 2021, *MNRAS*, **507**, 2550
- Skilling, J. 2004, in *AIP Conf. Proc. 735, Bayesian Inference and Maximum Entropy Methods in Science and Engineering*, ed. R. Fischer, R. Preuss, & U. V. Toussaint (Melville, NY: AIP), 395
- Skilling, J. 2006, *BayAn*, **1**, 833
- Smail, I., & Blundell, K. M. 2013, *MNRAS*, **434**, 3246
- Speagle, J. S. 2020, *MNRAS*, **493**, 3132
- Speranza, G., Balmaverde, B., Capetti, A., et al. 2021, *A&A*, **653**, A150
- Storchi-Bergmann, T., Dall’Agnol de Oliveira, B., Longo Micchi, L. F., et al. 2018, *ApJ*, **868**, 14
- Swinbank, A. M., Vernet, J. D. R., Smail, I., et al. 2015, *MNRAS*, **449**, 1298
- Temple, M. J., Banerji, M., Hewett, P. C., et al. 2019, *MNRAS*, **487**, 2594
- van Dokkum, P. G. 2001, *PASP*, **113**, 1420
- van Ojik, R., Roettgering, H. J. A., Miley, G. K., & Hunstead, R. W. 1997, *A&A*, **317**, 358
- Vayner, A., Zakamska, N. L., Ishikawa, Y., et al. 2024, *ApJ*, **960**, 126
- Veilleux, S., Liu, W., Vayner, A., et al. 2023, *ApJ*, **953**, 56
- Veilleux, S., Maiolino, R., Bolatto, A. D., & Aalto, S. 2020, *A&ARv*, **28**, 2
- Venemans, B. P., Kurk, J. D., Miley, G. K., et al. 2002, *ApJL*, **569**, L11
- Venturi, G., Nardini, E., Marconi, A., et al. 2018, *A&A*, **619**, A74
- Villar Martín, M., Emonts, B., Humphrey, A., Cabrera Lavers, A., & Binette, L. 2014, *MNRAS*, **440**, 3202
- Villar Martín, M., Emonts, B. H. C., Cabrera Lavers, A., et al. 2021, *A&A*, **650**, A84
- Villar-Martín, M., Arribas, S., Emonts, B., et al. 2016, *MNRAS*, **460**, 130
- Villar-Martín, M., Vernet, J., di Serego Alighieri, S., et al. 2003, *MNRAS*, **346**, 273
- Virtanen, P., Gommers, R., Oliphant, T. E., et al. 2020, *NatMe*, **17**, 261
- Wagner, A. Y., & Bicknell, G. V. 2011, *ApJ*, **728**, 29
- Wagner, A. Y., Bicknell, G. V., & Umemura, M. 2012, *ApJ*, **757**, 136
- Wang, F., Yang, J., Fan, X., et al. 2018, *ApJL*, **869**, L9
- Windhorst, R. A., Cohen, S. H., Jansen, R. A., et al. 2023, *AJ*, **165**, 13
- Zirm, A. W., Overzier, R. A., Miley, G. K., et al. 2005, *ApJ*, **630**, 68